

Stellar orbits in cosmological galaxy simulations: the connection to formation history and line-of-sight kinematics

Bernhard Röttgers^{1*}, Thorsten Naab¹ & Ludwig Oser²

¹*Max-Planck Institut für Astrophysik, Karl-Schwarzschild-Str. 1, 85741 Garching, Germany*

²*Department of Astronomy and Astrophysics, Columbia University, New York, NY 10027, USA*

Accepted ???. Received ??? in original form ???

ABSTRACT

We analyze orbits of stars and dark matter out to three effective radii for 42 galaxies formed in cosmological zoom simulations. Box orbits always dominate at the centers and z -tubes become important at larger radii. We connect the orbital structure to the formation histories and specific features (e.g. disk, counter-rotating core, minor axis rotation) in two-dimensional kinematic maps. Globally, fast rotating galaxies with significant recent *in situ* star formation are dominated by z -tubes. Slow rotators with recent mergers have significant box orbit and x -tube components. Rotation, quantified by the λ_R -parameter often originates from streaming motion of stars on z -tubes but sometimes from figure rotation. The observed anti-correlation of h_3 and V_0/σ in rotating galaxies can be connected to a dissipative formation history leading to high z -tube fractions. For galaxies with recent mergers *in situ* formed stars, accreted stars and dark matter particles populate similar orbits. Dark matter particles have isotropic velocity dispersions. Accreted stars are typically radially biased ($\beta \approx 0.2 - 0.4$). *In situ* stars become tangentially biased (as low as $\beta \approx -1.0$) if dissipation was relevant during the late assembly of the galaxy. We discuss the relevance of our analysis for integral field surveys and for constraining galaxy formation models.

Key words: stellar dynamics—orbital structure—galaxies: elliptical and lenticular, cD—galaxy formation.

* E-mail: broett@mpa-garching.mpg.de

1 INTRODUCTION

The observable properties of the stellar components of early-type galaxies (ETGs) result from the projected superposition of the light of individual stars with given ages and metallicities on particular orbits. Assuming that ETGs are in dynamical equilibrium the stars orbit in potentials which are mostly generated by the stars themselves but also by dark matter (at larger radii) and in some cases by additional gaseous components. Theoretically, a large number of equilibrium configurations can be constructed (see e.g. Binney & Tremaine 2008) but only a subset of all possible models seem to be realized in nature. Important information about the relevant formation and assembly processes of ETGs might therefore be stored in the orbital composition and the observable projected stellar line-of-sight kinematics.

Unlike for spiral galaxies, not all stars in present day massive ETGs have formed in the galaxy itself. It is more likely that the early formation ($z \gtrsim 2$) is dominated by *in situ* star formation and the late assembly becomes dominated by stellar accretion (see e.g. Khochfar & Silk 2006; Guo & White 2008; Naab et al. 2009; Oser et al. 2010; Feldmann et al. 2011; Lackner et al. 2012; Moster et al. 2013; Hilz et al. 2013). As dissipation is important during the early phase the systems are very likely axisymmetric and it is expected that stars will mostly form and move on tube orbits. Later on more and more stars (that have formed in other galaxies) are accreted in major and minor mergers and the final assembly of massive ETGs might be governed by collisionless dynamics alone. Mergers, however, can significantly change the orbital composition (and dynamics) of galaxies and direct information about the early assembly process might be hidden or lost (see e.g. Jesseit et al. 2005).

But also long after the main epoch of star formation gas can have a significant and observationally testable impact on the stellar morphology and kinematics. For example, it has been demonstrated by Barnes & Hernquist (1996) that during galaxy mergers gas can be driven to the central regions of the merger remnants making the central potential more axisymmetric. Such a configuration results in a more axisymmetric stellar shape, disfavors the population of stars on box orbits (which are the dominant orbit class for collisionless mergers (e.g. Jesseit et al. 2005)), and supports the population of minor axis tube orbits (Barnes & Hernquist 1996; Naab et al. 2006). This change in orbital configuration has a significant—and observable—impact on the line-of-sight kinematics of galaxies. Naab et al. (2006) showed that the presence of gas and the resulting change in orbital configuration changes the asymmetry of line-of-sight velocity profiles. Collisionless remnants show steep trailing (retrograde) wings (positive h_3) (Naab & Burkert 2001) whereas gas rich remnants have steep leading (prograde) wings (negative h_3) in much better agreement with observations (Naab et al. 2006; Hoffman et al. 2009, 2010).

Direct numerical cosmological simulations have become a valuable tool to understand galaxy formation and are a major driver for theoretical scientific progress in the field. It is now possible to follow the evolution of individual galaxies over a Hubble time at high resolution, starting to resolve the internal stellar structure of galaxies (see e.g. Naab et al. 2007) and study the impact of feedback processes on galaxy dynamics. For example, it has been demonstrated

that simulations with identical initial conditions, but different feedback models can yield galaxies with significantly different morphological and kinematic properties (e.g. Piontek & Steinmetz 2011; Scannapieco et al. 2012; Puchwein & Springel 2013; Hirschmann et al. 2013; Aumer et al. 2013). Any form of ‘feedback’ directly affects the distribution and thermodynamic properties of the dissipative component (gas) in and around galaxies and thereby regulates when and where stars are formed—determining their initial orbits—and how much gas is funneled to the centers or expelled from the galaxies at which stage of their evolution. For the same initial conditions, stronger feedback in general leads to more *in situ* star formation, higher gas fractions, and less stellar accretion at late times (Hirschmann et al. 2012; Lackner et al. 2012; Hirschmann et al. 2013). This will also lead to a changes in the orbital composition at the present day.

In this paper we provide the framework for a fast and self-consistent analysis of stellar orbits in high-resolution cosmological zoom simulations similar to Jesseit et al. (2005). We focus on a set of cosmological simulations with weak stellar feedback and test for correlations with global and detailed observable properties. The impact of feedback on our results will be presented in a follow-up study. In a larger scale cosmological context, Bryan et al. (2012) have presented a similar study on the orbital content of dark matter halos of simulations with different feedback and radiative cooling models and indeed found the orbital content of the halo to change strongly with different feedback models.

In addition to the pure identification of the stellar orbits we connect this information with observable properties showing up in two-dimensional kinematic maps (see also Naab et al. (2013)). This information provides direct theoretical input for the results from existing and upcoming integral-field surveys like e.g. SAURON (Bacon et al. 2001), ATLAS^{3D} (Cappellari et al. 2011), KMOS (Sharples et al. 2006), VIRUS-P (Hill et al. 2008), CALIFA (Sánchez et al. 2012), SAMI (Fogarty et al. 2012), SLUGGS (Arnold et al. 2014), MASSIVE (Ma et al. 2014) or MANGA. Our results will help to understand how the assembly history of a galaxy influences its orbital content and the observable line-of-sight velocity distributions (LOSVDs) which are extracted from the survey data.

The paper is organized as follows: We briefly review the simulations in Section 2 and present our analysis procedure including the reconstruction of the potential, the orbit classification and the construction of LOSV maps in Section 3. In Section 4 we present results on the connection of orbit classes with triaxiality, line-of-sight kinematics, LOSVD asymmetries, and the two-phase assembly process. We summarize and discuss our results in Section 5.

2 SIMULATIONS

In this paper we investigate the orbital structure of central galaxies of the cosmological hydrodynamic zoom simulations presented in Oser et al. (2010). This sample of simulations (or parts of it) has been used to study cosmological size and dispersion evolution (Oser et al. 2012), the mass distribution (Lyskova et al. 2012) as well as the detailed two-dimensional kinematic properties at small (Naab et al. 2013) and large

radii (Wu et al. 2014). The galaxies have present-day stellar masses ranging from $6.1 \times 10^{10} M_\odot$ to $6.9 \times 10^{11} M_\odot$.

The simulations were performed using GADGET (Springel et al. 2001; Springel 2005) with cosmological parameters based on the three year results of the Wilkinson Microwave Anisotropy Probe (WMAP) (Spergel et al. 2007): $\sigma_8 = 0.77$, $\Omega_m = 0.26$, $\Omega_\Lambda = 0.74$, $h = 0.72$ and $n_s = 0.95$. The halos of interest were drawn from a large-scale dark matter run with 512^3 ($\approx 10^8$) particles in a cube with co-moving side length of $72 \text{ Mpc } h^{-1}$ from redshift $z \simeq 43$ to $z = 0$ with a fixed gravitational smoothing length of $2.52 \text{ kpc } h^{-1}$ and a mass of $m_p = 2 \times 10^8 M_\odot$ per particle (see Moster et al. (2010)).

All particles of the halos of interest within $2 \times R_{200}$ at $z = 0$ were traced back to the beginning of the simulation. A region enclosing all these particles at $z \simeq 43$ then was populated with dark matter and gas particles ($\Omega_{\text{dm}} = 0.216$ and $\Omega_b = 0.044$) with smoothing lengths reduced to $0.89 \text{ kpc } h^{-1}$ and $0.4 \text{ kpc } h^{-1}$, respectively. The particle masses were $m_{*,\text{gas}} = 4.2 \times 10^6 M_\odot$ for star and gas particles and $m_{\text{dm}} = 2.5 \times 10^7 M_\odot$ for dark matter particles. Outside this region and beyond a ‘safety margin’ of $1 \text{ Mpc } h^{-1}$ the original dark matter particles were down-sampled depending on the distance with sufficient resolution to represent long range forces.

The simulations include the effect of a redshift-dependent uniform UV background, radiative cooling, star formation, and energy feedback from type-II supernovae using the model of Springel & Hernquist (2003). As discussed in Oser et al. (2010, 2012) this sub-grid model favors the efficient conversion of gas into stars at high redshifts and supports the formation of spheroidal systems. However, the massive galaxies forming with this particular sub-grid model have structural properties that agree reasonably well with observed ellipticals (see also Naab et al. 2007; Johansson et al. 2012; Lyskova et al. 2012; Naab et al. 2013; Wu et al. 2014). An overview of some global galaxy properties is given in Tab. 2 along with the global orbit fractions determined later in this work.

3 ANALYSIS

3.1 Galaxy identification and orientation

At $z = 0$, we identify galaxies (including their dark matter halos) with a friends-of-friends algorithm and determine their centers in configuration space (position and velocity) using a shrinking sphere technique (Power et al. 2003). The central galaxies are then defined by all baryonic particles within R_{10} , i.e. 10% of the virial radius $R_{\text{vir}} \equiv R_{200}$.

The orbit classification scheme (see Section 3.3) requires the galaxies—or more precisely their potentials—to be oriented along their principal axes. Only a few degrees of misalignment can change the exact orbit fractions. We use the method presented in Bailin & Steinmetz (2005) to compute the ‘reduced inertia tensor’ $\tilde{\mathbf{I}}$,

$$\tilde{I}_{ij} = \sum_{\text{Particles } k} m_k \frac{r_{k,i} r_{k,j}}{r_k^2}, \quad (1)$$

where m_k are the masses and \vec{r}_k are the positions of the individual stellar particles within a given radius; in this work

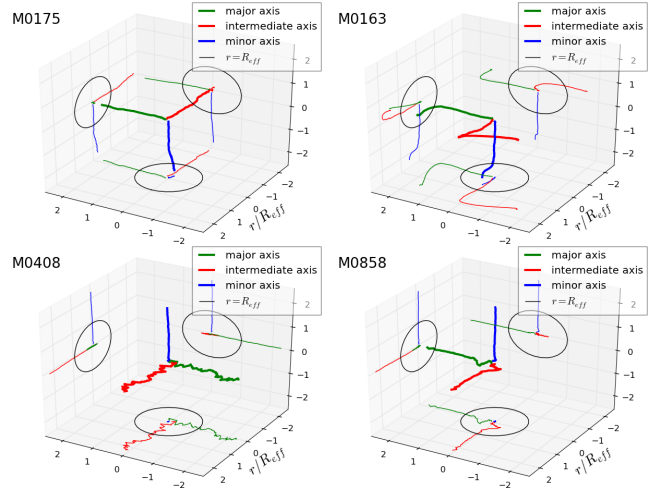


Figure 1. The orientation of the eigenvectors of the reduced inertia tensor as a function of radius. The black circles on the projections indicates the effective radius. Most galaxies like M0175 and M0163 show good internal alignment and the orientation of the reduced inertia tensor only changes at larger radii, where large substructures are (cf. M0163). Some very axisymmetric galaxies like M0408 have radially fluctuating eigenvectors in the plane perpendicular to the symmetry axis. Only very few simulated galaxies show internal misalignment within R_{eff} , like M0858.

within the half mass radius of the stars. The eigenvectors of this tensor then give the orientation of the principal axes.

An advantage of this method over the traditional moment-of-inertia tensor is that it weighs particles at different distances from the center equally, whereas the normal moment-of-inertia tensor, $I_{ij} = \sum_k m_k (\delta_{ij} r_k^2 - r_{k,i} r_{k,j})$, weighs masses m_k with $\mathcal{O}(r_k^2)$. We, however, would like to determine the orientation of the potential, whose depth is proportional to the mass, and hence the reduced inertia tensor is more appropriate. For example massive substructures at large radii would dominate the normal inertia tensor due to the $\mathcal{O}(r^2)$ -factor, whereas the potential would still be dominated by the galaxy at small radii.

For most galaxies the orientation of the principal axes defined via $\tilde{\mathbf{I}}$ does not vary significantly within the effective radius¹ (see Fig. 1). Only a few galaxies show internal twists or misaligned cores like M0858. Galaxies that are almost axisymmetric like M0408 have the principal axis of the reduced inertia tensor perpendicular to the symmetry axis fluctuating with the radius up to which $\tilde{\mathbf{I}}$ was determined. However, the potential is axisymmetric as well and thus it does not compromise the classification.

Substructures, that are massive enough to significantly impact the potential (basically on-going/up-coming mergers) and the direction of the principal axis—like for M0163—, typically are located beyond R_{eff} .

We also compute the triaxiality parameter,

$$T = \frac{1 - (b/a)^2}{1 - (c/a)^2}. \quad (2)$$

¹ In this work we assume a constant light-to-mass ratio and we ignore gas. Hence, the effective radius is simply the half-mass radius of the stars.

Here a is the major axis, b the intermediate axis and c the minor axis. The two axis ratios can be calculated from the square roots, $\tilde{a} > \tilde{b} > \tilde{c}$, of the eigenvalues of the reduced inertia tensor (Bailin & Steinmetz 2005):

$$\left(\frac{c}{a}\right) \simeq \left(\frac{\tilde{c}}{\tilde{a}}\right)^{\sqrt{3}} \quad \text{and} \quad \left(\frac{b}{a}\right) \simeq \left(\frac{\tilde{b}}{\tilde{a}}\right)^{\sqrt{3}}. \quad (3)$$

3.2 Reconstruction of the potential

To classify the orbits of the stellar particles we need to know their trajectories—at high temporal resolution—in the potential of the galaxy. To speed up the orbital classification we freeze the system at redshift zero, use a self-consistent field method (SCF, Hernquist & Ostriker 1992) to extract the potential, and then integrate the individual orbits of the particles we would like to classify (for a similar approach see Jesseit et al. 2005; Naab et al. 2006; Hoffman et al. 2009; Bryan et al. 2012).

We have investigated two different basis functions for the potential expansion. The first one (CB hereafter) was presented in Clutton-Brock (1973). At zeroth order it is the density and potential of a Plummer sphere,

$$\rho(r) = \frac{3M}{4\pi a^3} \left(1 + \frac{r^2}{a^2}\right)^{-5/2},$$

$$\phi(r) = -\frac{GM}{\sqrt{r^2 + a^2}},$$

where M is the total mass and a is the scale parameter. Another set of SCF basis functions (HO hereafter) was suggested by Hernquist & Ostriker (1992), for which the zeroth order density and potential are

$$\rho(r) = \frac{M}{2\pi} \frac{a}{r} \frac{1}{(r+a)^3},$$

$$\phi(r) = -\frac{GM}{r+a}.$$

This is the Hernquist density profile (Hernquist 1990) which is a popular model for representing spheroidal galaxies (e.g. Hilz et al. 2013) and resembles a de Vaucouleur’s $R^{1/4}$ surface density profile (see however Naab & Trujillo 2006).

For both basis functions the difference of the real (simulated) potential and the zeroth order term is expanded in a bi-orthogonal basis set built-up from the spherical harmonics and a radial basis set. The better the first order terms follow the underlying model, the less terms in the basis set expansion are needed to produce a good approximation to the original potential. We have tested both basis set for varying radial and angular expansion terms and in all cases we find that the HO basis set results in a significantly better representation of the potential as it does not have a flat density core inside the scale radius. In Fig. 2 we give an example of the potential reconstruction for galaxy M0163. The SCF potential and the potential from the simulation agree very well. In addition, substructures at larger radii are washed out which results in a smoother overall potential and makes the orbit classification more stable. At the center, the HO basis set represents the potential much better than the CB basis set (bottom panel of Fig. 2). Moreover the quality of the HO fit is less sensitive to the choice of the scale parameter a and the typical relative error of this basis set assuming a radial order $n_{\max} = 18$ and an angular order $\ell_{\max} = 7$ is

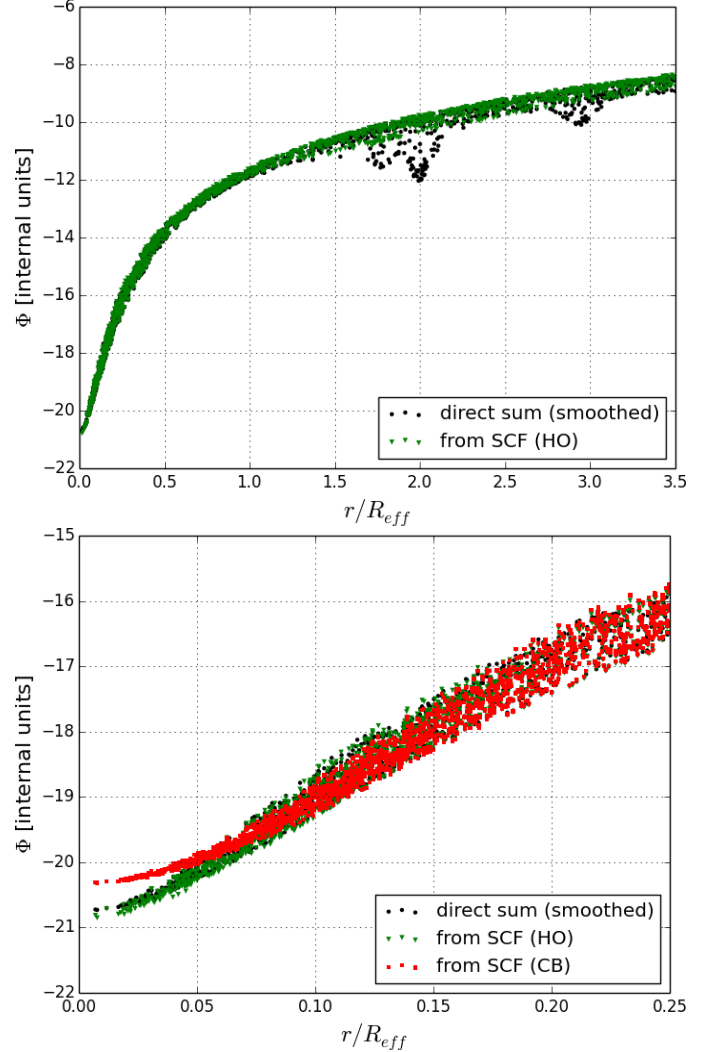


Figure 2. *Top panel:* Comparison of the potential extracted from the particle distribution (black dots) and the SCF potential with a HO basis function set ($n_{\max} = 18, \ell_{\max} = 7$, green triangles) of galaxy M0163 for a set of randomly chosen stars. The fitted potential agrees well at the center and substructures at large radii are smoothed out. *Bottom panel:* Comparison of the direct (black) and HO (green triangles) potential to a fit using the CB basis functions (red squares) using the same radial and angular order. At a fixed order the HO basis set fits the central potential much better.

less than 0.5%. Hence, we use the HO basis function set to reconstruct the potential of all simulated galaxies.

3.3 Orbit classification

In integrable systems bound orbits are confined on manifolds of phase space that are topologically equivalent to tori. This allows one to describe them with angle-action variables (θ, \mathbf{J}) in which the equations of motion become

$$0 = \dot{J}_i = -\frac{\partial \mathcal{H}}{\partial \theta_i} \quad (4)$$

$$\dot{\theta}_i = -\frac{\partial \mathcal{H}}{\partial J_i} =: \Omega_i(\mathbf{J}), \quad (5)$$

where \mathcal{H} is the Hamiltonian. The Ω_i are called fundamental frequencies and are conserved quantities. It can be shown that real space trajectories $\mathbf{x}(t)$ are quasi-periodic, i.e. they can be written in a Fourier series,

$$\mathbf{x}(t) = \sum_{\mathbf{n} \in \mathbb{N}^3} \mathbf{X}_{\mathbf{n}}(\mathbf{J}) e^{i\mathbf{n} \cdot \boldsymbol{\theta}(t)}, \quad (6)$$

with constant amplitudes $\mathbf{X}_{\mathbf{n}}$ and linearly growing angles $\boldsymbol{\theta}(t) = \boldsymbol{\theta}(0) + \boldsymbol{\Omega} \cdot t$. Such quasi-periodic orbits are also called regular orbits.

Galaxies do not have to be integrable systems. However, orbit theory and in particular KAM theory (see e.g. Kolmogorov 1954, 1979; Moser 1973; Arnol'd 1989; Binney & Tremaine 2008; Arnol'd et al. 2007) tell us, that near-integrable systems (whose Hamiltonian differs only slightly from an integrable Hamiltonian) still have ‘islands’ of regular orbits next to their otherwise irregular/chaotic orbits. The smaller the deviation of the Hamiltonian from an integrable one, the larger these island are.

It turns out that regular orbits can be classified into four different main classes, depending on the ratios of the Ω_i (see e.g. de Zeeuw 1985; Statler 1987; Binney & Tremaine 2008): box orbits, minor-axis orbits (we call them z -tubes for short) and inner and outer major-axis orbits (x -tubes for short, see Fig. 4). These classes have fundamentally different physical properties. Box orbits have no mean angular momentum and are typically centrophilic, whereas all tube orbits are centrophobic and have a net angular momentum which is either aligned with the z -axis (for z -tubes) or with the x -axis (for x -tubes). They also have different, often interesting geometries (e.g. the ‘boxlet’ in Fig. 4).

Carpintero & Aguilar (1998) (CA98 hereafter) developed a classification scheme, that almost entirely builds on the detection of resonances (only inner and outer x -tubes have to be distinguished morphologically). z -tubes, for instance, have a 1:1 resonance in the two dominant frequencies in the x - and the y -coordinate. CA98 have also written a program to automatically classify orbits by using the Fourier transforms of the trajectories (in three dimensions), detecting the most prominent lines and then checking these lines for resonances. Depending on the number of base frequencies² that are needed to build up the detected lines (by their linear combinations) and the number and kind of resonances the orbits are classified (see Tab. 1).

This scheme is capable of differentiating between z -tubes, x -tubes, non-resonant box orbits—so called ‘ π -boxes’—and resonant box orbits (all resonance apart from 1:1 resonances)—called ‘boxlets’—, as well as second order resonances. These occur when a particle is oscillating resonantly around a stable, already resonant orbit. We, however, only make use of the differentiation between the main orbit classes (boxes, z -tubes, x -tubes, irregulars) and non-classified orbits.

The basic classification procedure works as follows: first we integrate the particles, starting from their coordinates and velocities at $z = 0$ in the reconstructed SCF potential

² Base frequencies are very similar to the fundamental frequencies, but not necessarily the same. It might be that one of them is twice the corresponding fundamental frequency, for instance, and the amplitude of uneven multiples of the fundamental frequency are undetectable small.

		number of base frequencies		
		< 3	= 3	3 <
number of resonances	0	low dim. (closed and thin) orbits	3-D π -box	irregular
	1		open $\pi:m:n$ box open $\pi:1:1$ tube	
	3		open $l:m:n$ box open $l:1:1$ tube	

Table 1. Summary of the spectral orbit classification in three dimensions as defined in Carpintero & Aguilar (1998). Chaotic orbits have more than three base frequencies; regular orbits are classified according to their resonance: tubes, boxlets ($\pi:m:n$ or $l:m:n$ boxes) or (non-resonant) π -boxes. Depending on whether their trajectories fill a three dimensional volume (‘open’ orbits) or a lower dimensional one, they have three or less base frequencies, respectively.

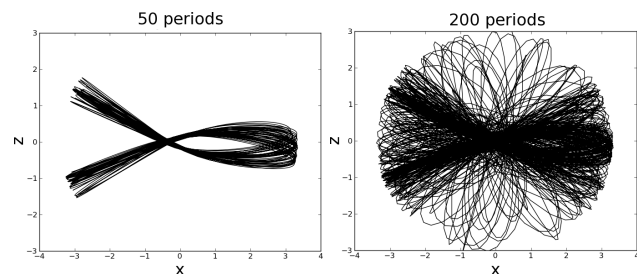


Figure 3. An example for a ‘sticky’ orbit: A star particle of galaxy M0175 looks like a regular ‘fish orbit’ (a 2:3-resonance, left panel) if integrated for 50 orbital periods (~ 7.5 Gyrs). After longer integration for 200 periods (~ 30 Gyrs) the orbit shows its irregular nature (right panel). For the classification in this paper all orbits are integrated for $\lesssim 50$ orbital periods.

with a Runge-Kutta integrator of 8th order with adaptive time steps (capable of continuous on-the-fly output). We require a relative accuracy in position and velocity of 10^{-8} per step, which leads to relative changes in the particles’ energies of order 10^{-5} . The CA98 code then actually classifies an orbit three times using slightly different parts of the trajectory. If all three classifications differ the particle counts as ‘not classified’.

The orbit classification for the almost 3×10^6 star particles in this work would have taken several months with the original serial code. Therefore we have parallelized the loop over the particles with OpenMP and with that reduced the computation time to a couple of days. In addition, we added a module to estimate the orbital period of each particle before the final classification to ensure that it is integrated for a fixed number of orbital periods rather than a fixed global integration time. The orbital periods vary significantly with radius / binding energy for a typical galaxy: close to the centers we find orbital periods less than 10 Myr and at $3 R_{\text{eff}}$ they can be longer than 1 Gyr.

The orbital period is usually defined as the inverse of the dominant frequency along the major axis. To first order, the particle should pass the y - z -plane twice for each period. To get an estimate for the orbital period of each particle we first integrate (with low accuracy) until the desired orbital periods sign changes (corresponding to ~ 40 periods) have occurred. We then terminate the integration and then re-integrate the orbit for the same time at high accuracy for the orbit classification.

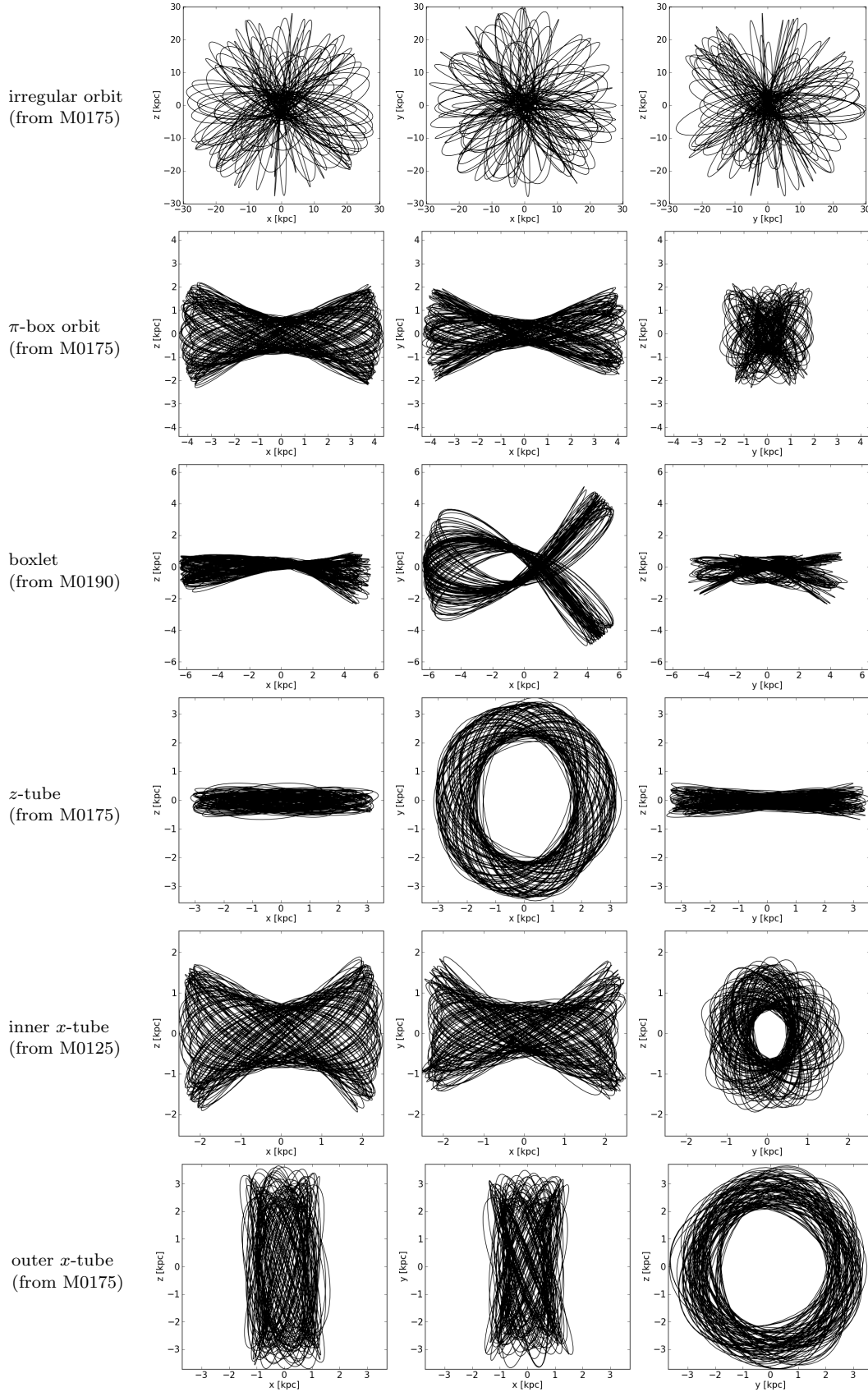


Figure 4. Selected examples of the most regular trajectories (for three projections along the principal axes, from left to right) of the main orbit classes for individual particles taken from different simulated galaxies complemented with one very chaotic/irregular orbit. All tube orbits are centrophobic, while box orbits and irregular orbits can go through the center.

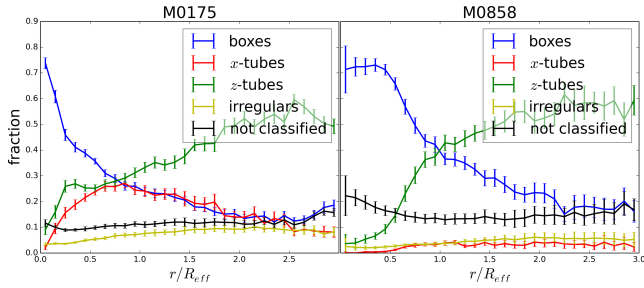


Figure 5. Orbit fractions as a function of radius for a bootstrapping ensemble of realizations of two representative galaxies, M0175 and M0858. Solid lines are the mean of 50 bootstrapped realizations the errorbars indicate the standard deviations. The uncertainties due to the coarse sampling of phase space are small.

To find an optimal integration time, the trajectory has to be sufficiently long to detect peaks and their resonances in the Fourier spectra. On the other hand, too long integration time leads to inaccuracies and the sampling with the FFT can become too coarse to detect low amplitude frequencies. A complication are so-called ‘sticky orbits’, irregular orbits that come near to a resonantly trapped region in phase space, stick to it for some time and drift away slowly. These orbits look and behave very similarly to the resonant orbits nearby. Their actual irregular nature is not revealed until they have drifted away from the resonance (see Fig. 3), which in many cases requires integration for much more than the Hubble time. An appropriate integration time ensures that these orbits are classified as regular orbits. The classification is most robust if we integrate for about 40 – 50 periods (which is shorter than the 100 periods as suggested by CA98 for a more detailed analysis).

3.4 Stability of the orbit classification

In this section we present test of how well the potential is sampled and how the sampling affects the orbit classification. For this we use the bootstrapping technique (see Heyl et al. 1994; Naab & Burkert 2003). From the original ensemble of particles, we randomly draw the same number of particles with replacement. This is done separately for each particle species (gas, stars, and dark matter) to maintain the mass of each component.

We analyse 50 different realizations for two representative galaxies without figure rotation (M0175 and M0858). In Fig. 5 we show the mean orbit fractions and the variations (standard deviations) indicated by the error bars. The orbit classification is very robust and hardly affected by the sampling of phase space. The variations are typically small for the stellar component and can increase slightly at large radii ($r > 2R_{\text{eff}}$; see Wu et al. 2014 for the effect of time averaging the potential to measurements at large radii). Most importantly, none of the conclusion in the paper are affected by sampling issues. The small variations in orbit fractions are caused by individual particles that change orbit families asymmetrically (see also Sec. 3.3) for different realizations of the potential. Typically almost 90% of the particles in the main orbit families do not change classification.

In Fig. 6 we investigate the evolution of orbit fractions in time for the last five snapshots covering about 500 Myrs.

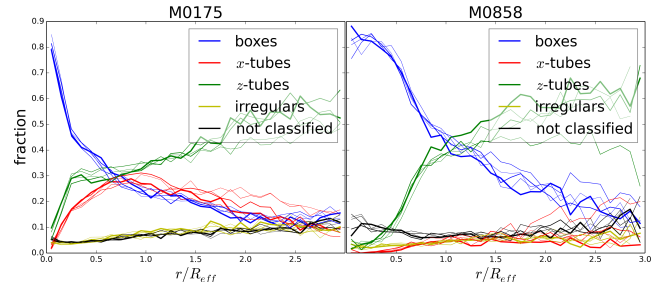


Figure 6. The time evolution of the orbit fractions as a function of radius for the last five snapshots (~ 0.5 Gyrs; the first snapshot is indicated by a thick line) for the same galaxies as in Fig. 5. The fractions are stable with moderate fluctuations at large radii ($r > 2R_{\text{eff}}$).

Again for both galaxies the orbit fractions are stable for the main part of the galaxies. At larger radii ($r > 2R_{\text{eff}}$) the fluctuations with time become larger due to moving substructures (e.g. M0858).

In summary, the orbit fractions presented in section 4 are reliable and stable for a few dynamical times. Therefore none of the conclusions in the paper are affected by sampling issues and time evolution of the modelled galaxies.

3.5 Figure rotation

Since we have fixed the potential using a time-independent SCF potential, the classification procedure does not account for the possibility of a rotating figure. Some of our galaxies, however, show clear signs of figure rotation. We find that the systems that rotate are rather prolate or have bar-like structures that rotate.

The rotation of the figure is also imprinted in the motion of the stars. Using the classification scheme without caution would lead to an incorrect orbit classification. Hence, we excluded galaxies that show signs of figure rotation from our orbit analysis. These are M0380, M0549, M0763, M0858, M1192 and M1306.

A direct integration of rotating figure into the CA98 classification scheme would be very demanding or even impossible, because a) the measurement of figure rotation is quite error-prone, b) the amount of figure rotation can change a lot over time due to external torques and c) figure rotation can be differential. The latter point means that the principal axis (of the reduced inertia tensor) change with radius and time. This not only complicates the methods of classification but a static potential is actually a premise of orbit theory. Hence, we restrict ourselves to galaxies with slowly varying/rotating potentials. In order to check the robustness of the classification in slowly rotating potentials, we added small amounts of rigid rotation to the SCF potentials and found that the orbit composition within a few effective radii does not change much for moderate pattern speeds. Therefore we trust the classification for all but the excluded galaxies.

3.6 Line-of-sight kinematics

To connect the orbital structure of the galaxies to their line-of-sight kinematics we present two-dimensional maps of the

LOS velocity, and dispersion as well as h_3 (see below). The maps are constructed in a similar way to observations and all details can be found in Naab et al. (2013). Here we just give a short summary. In a first step the galaxies are oriented along their principal axes and projected along the intermediate axis, resulting in an edge-on view. We split each stellar particle into 60 pseudo-particles with a Gaussian distribution of standard deviation 0.3 kpc. The pseudo-particles are gathered into Voronoi bins such that each final bin has a signal-to-noise ratio of about 40 (Cappellari & Copin 2003).

For each bin the line-of-sight velocity profile $P(v)$ is fitted (van de Ven et al. 2006) with Gauss-Hermite functions following Gerhard (1993) and van der Marel & Franx (1993), using terms up to the fourth order:

$$P(v) = \frac{\gamma}{\sqrt{2\pi}\sigma^2} e^{-\frac{w^2}{2}} \left(1 + h_3 H_3(w) + h_4 H_4(w)\right), \quad (7)$$

where

$$w \equiv \frac{v - V_0}{\sigma} \quad (8)$$

is the normalized deviation of the velocity from the mean velocity V_0 , and H_3 and H_4 are Gauss-Hermite polynomials. γ is a normalization parameter and also one of the fitting parameters ($\gamma, V_0, \sigma, h_3, h_4$). The amplitude h_3 of the third order term is connected to the skewness and h_4 is a measure of the kurtosis of the velocity profile. Skewness and kurtosis, however, are more sensitive to statistical deviations at the far ends of the wings (van der Marel & Franx 1993).

We also calculate the λ_R -parameter as introduced by Emsellem et al. (2007, 2011), a luminosity weighted measure of rotation:

$$\lambda_R = \frac{\sum_{i=1}^N F_i r_i |V_{0,i}|}{\sum_{i=1}^N F_i r_i \sqrt{V_{0,i}^2 + \sigma_i^2}}, \quad (9)$$

where F_i is the flux (which here is the mass of the stars, for a constant light-to-mass ratio) in bin i of the projected galaxy, r_i is its projected radius, $V_{0,i}$ is the line-of-sight velocity and σ_i is the line-of-sight velocity dispersion of bin i .

4 RESULTS

4.1 Orbit population and triaxiality

We classify the orbits for stellar and dark matter particles up to 3 effective radii for all 42 galaxies (a summary is given in Tab. 2). The particles populate all major orbit classes: box orbits and boxlets (boxes), z -tubes (minor-axis loop orbits), inner and outer x -tubes (major-axis loop orbits), and irregular orbits (see Fig. 4). In general, the dominant orbit families are boxes and z -tubes, sometimes x -tubes, with significant radial variation. A small fraction of the orbits, typically less than $\sim 10\%$, are irregular or cannot be classified.

In Fig. 7 we show the radial orbit distribution for six galaxies that belong to distinct formation classes as discussed in Naab et al. (2013). M0721 (upper left panel in Fig. 7) is a fast rotating galaxy with gas-rich minor mergers only (class A) and M0408 (upper middle panel in Fig. 7) is a fast rotating remnant of a major merger with dissipation (class B). Both are dominated by z -tubes, apart from the very center ($r \lesssim 0.25R_{\text{eff}}$). Such an orbit structure is very generic for galaxies of class A and B and it is very similar to

gas-rich major mergers (see e.g. Naab et al. 2006; Hoffman et al. 2010).

A slowly rotating gas-rich merger remnant (M0664, class C) is shown in the upper right panel of Fig. 7. This galaxy is triaxial, almost prolate ($T \simeq 0.6 - 0.7$), with a significant population of major axis tubes inside one effective radius. Again, this galaxy is dominated by minor-axis tubes at large radii. M0163 is a fast rotating remnant of a gas-poor major merger (class D, bottom left panel of Fig. 7) and is dominated by box orbits, in particular at the center and at large radii (though the box orbits in the outer parts are mostly from a substructures there). An example for a slowly rotating remnant of a gas-poor major merger (class E) is shown in the middle bottom panel of Fig. 7. M0190 is again dominated by box orbits at the center, however, at large radii box orbits, z -tubes and x -tubes contribute equally. M0175, a massive galaxy assembled by minor mergers since $z \approx 2$ (class E), is dominated by boxes at the center and minor-axis tubes in the outer parts with a significant major-axis tube contribution at all radii (bottom right panel of Fig. 7).

For all fast rotating galaxies of classes A and B (like M0721 and M0408) the orbit distributions are generic. All other galaxy classes show significant variations in the orbit distributions. For example not all galaxies of class D have such high box fraction at large radii as M0163. Still, we do find trends, in particular around the effective radius, $0.5 \lesssim R_{\text{eff}} \lesssim 1.5$ (see Fig. 8). Fast rotators (classes A, B, and D) tend to have more z -tubes than the other classes, in particular classes A and B. In slow rotators (classes C, E, and F) box orbits are more abundant. Also, x -tubes are rare in fast rotators. However, a high z -tube fraction is not the only factor determining the amount of rotation as we will show in section 4.2. A common feature for all galaxies of the radial orbit distributions is a very box orbit dominated center (typically more than 60% are boxes). This can probably be ascribed to the simulation model we use as we will discuss later.

It has been shown that the orbital composition (orbit fractions) correlate with the three-dimensional shape (triaxiality) of the system (Statler 1987; Jesseit et al. 2005). In Fig. 9 we show z -tube, x -tube, and box orbit fractions as a function of triaxiality of the galaxies. As expected, z -tubes preferentially live in oblate ($T \approx 0$) systems, where they can rotate around a well-defined minor axis, which is poorly defined in a prolate ($T \approx 1$) system. In a galaxy with $T = 1$ exactly there are no z -tubes at all. x -tubes are most abundant in prolate systems with a well-defined major axis (x -axis) and the abundance of box orbits peaks roughly at the most triaxial systems ($T \approx 0.5$, see right panel of Fig. 9). The fact that all systems have at least 20% box orbits indicates that none of the systems is perfectly oblate.

4.2 Orbits and line-of-sight kinematics

In Fig. 10 we directly compare the orbital structure of the six example galaxies to the two-dimensional (edge-on) line-of-sight velocity and velocity dispersion maps up to $1.5R_{\text{eff}}$. z -tubes are the only orbits with a definite sense of rotation around the minor axis, and one expects a high line-of-sight velocity (along the major-axis) at z -tube dominated radii. This can be seen for M0408 and M0163.

ID	M_* [$10^{10} M_\odot$]	R_{eff} [kpc]	triax. T	λ_R	<i>in situ</i> frac.	box frac.	z -tube frac.	x -tube frac.	Eff. prograde z -tube frac.
M0040	49.98	12.92	0.69	0.13	0.11	0.44	0.24	0.12	0.04
M0053	69.45	13.03	0.51	0.093	0.19	0.29	0.40	0.17	0.02
M0069	49.40	8.84	0.68	0.15	0.15	0.43	0.22	0.19	0.09
M0089	52.34	10.43	0.45	0.074	0.084	0.44	0.27	0.11	0.03
M0094	47.90	7.53	0.54	0.098	0.16	0.38	0.39	0.13	0.12
M0125	43.35	9.07	0.85	0.078	0.12	0.26	0.17	0.48	0.02
M0162	36.44	9.78	0.80	0.074	0.081	0.52	0.19	0.13	0.06
M0163	35.20	10.39	0.63	0.31	0.098	0.49	0.25	0.10	0.12
M0175	36.79	7.37	0.58	0.058	0.14	0.34	0.35	0.19	0.01
M0190	31.48	6.98	0.77	0.083	0.093	0.51	0.18	0.17	0.01
M0204	26.85	6.49	0.37	0.10	0.12	0.31	0.45	0.12	0.06
M0209	19.96	3.81	0.41	0.14	0.17	0.46	0.36	0.06	0.09
M0215	27.64	5.04	0.49	0.14	0.16	0.33	0.32	0.25	0.10
M0224	24.84	5.95	0.26	0.16	0.14	0.24	0.54	0.10	0.11
M0227	30.90	7.91	0.61	0.24	0.10	0.35	0.38	0.16	0.18
M0259	19.83	4.53	0.06	0.40	0.15	0.28	0.58	0.02	0.30
M0290	22.03	3.57	0.10	0.48	0.19	0.18	0.73	0.03	0.47
M0300	18.65	4.58	0.37	0.19	0.12	0.42	0.40	0.05	0.17
M0305	25.76	8.92	0.46	0.12	0.11	0.50	0.21	0.11	0.01
M0329	21.33	4.32	0.49	0.071	0.16	0.44	0.29	0.16	0.03
M0380	17.08	4.04	0.57	0.46	0.17	0.44	0.34	0.10	0.15
M0408	17.71	3.60	0.07	0.37	0.20	0.23	0.67	0.02	0.34
M0443	23.08	2.74	0.44	0.088	0.24	0.37	0.42	0.14	0.11
M0501	16.31	4.29	0.55	0.075	0.16	0.47	0.23	0.15	0.05
M0549	11.64	4.66	0.33	0.46	0.17	0.44	0.31	0.09	0.16
M0616	13.04	4.07	0.72	0.077	0.16	0.47	0.19	0.21	0.02
M0664	10.39	2.91	0.64	0.14	0.17	0.33	0.34	0.23	0.00
M0721	13.35	2.32	0.14	0.40	0.38	0.29	0.60	0.02	0.24
M0763	13.68	4.28	0.30	0.32	0.099	0.39	0.43	0.06	0.25
M0858	14.26	2.69	0.31	0.52	0.32	0.50	0.35	0.03	0.18
M0908	13.43	2.83	0.06	0.44	0.38	0.20	0.69	0.01	0.38
M0948	9.23	4.75	0.69	0.088	0.12	0.31	0.20	0.35	0.03
M0959	8.41	2.94	0.88	0.091	0.18	0.31	0.13	0.46	0.03
M0977	6.32	3.26	0.47	0.35	0.37	0.47	0.26	0.11	0.16
M1017	8.87	2.27	0.61	0.084	0.29	0.46	0.33	0.12	0.04
M1061	7.20	3.13	0.64	0.066	0.21	0.54	0.16	0.17	0.02
M1071	10.82	2.37	0.50	0.14	0.21	0.32	0.40	0.20	0.12
M1091	10.46	2.00	0.54	0.040	0.25	0.57	0.25	0.09	0.02
M1167	10.24	2.31	0.54	0.062	0.26	0.55	0.25	0.11	0.07
M1192	6.05	2.64	0.69	0.50	0.20	0.54	0.18	0.16	0.11
M1196	10.74	3.04	0.11	0.45	0.33	0.27	0.61	0.01	0.41
M1306	9.04	1.84	0.13	0.59	0.28	0.39	0.50	0.03	0.31

Table 2. Properties of simulated galaxies: M_* is the stellar mass of the galaxy, i.e. the stellar mass within $10\% R_{200}$, R_{eff} is the half mass radius of the galaxy’s stars (i.e. the effective radius assuming a constant mass-to-light ratio and ignoring gas), the triaxiality T is measured at R_{eff} , λ_R is the rotational parameter as defined in formula 9, the *in situ* fraction is the fraction of the stars that were formed *in situ* since $z = 2$ and the orbit class fractions were determined with the modified CA98 classifier within $3R_{\text{eff}}$. The effective prograde z -tube fraction is defined as the difference between the prograde and the retrograde z -tube fraction. Uncertain orbit fractions for galaxies with significant figure rotation are given in grey.

However, not all particles on z -tube orbits have to rotate in the same direction and the net-rotation can cancel out, resulting in slow rotation like for M0664, M0190 and M0175, with a slightly higher velocity dispersion. To investigate this effect, we separated the z -tubes into prograde (co-rotating) and retrograde (counter-rotating) orbits and plot the prograde z -tube fractions (green dashed lines in the orbit fraction plots) in Fig. 10. Wherever they dominate the z -tube population (M0408, and M0163), the galaxy is clearly rotating. Similar trends also hold for x -tubes, however, M0190 is the only galaxy in the sample with noticeable major-axis rotation, which is why we concentrate on minor axis rotation.

We demonstrate the direct connection between the or-

bit composition and the line-of-sight kinematics by performing a separate analysis for stars on different orbit classes. In Fig. 11 we show the line-of-sight kinematics for M0408 for the full stellar population, and for the stars on box orbits, z -tubes, and x -tubes respectively (from top left to bottom right). For this galaxy the rotation originates from the dominant population (66.4 %) of z -tubes, whereas boxes (23.9 %) and x -tubes (1.9 %) show no (significant) rotation, typical for most fast rotators. Also the disk-like component, visible in the isodensity contours, is composed of stars on z -tubes. The box orbits contribute to the central dispersion, whereas the dispersion at R_{eff} is almost entirely determined by z -tubes.

Slow rotators like M0175 (Fig. 12) have a non-rotating

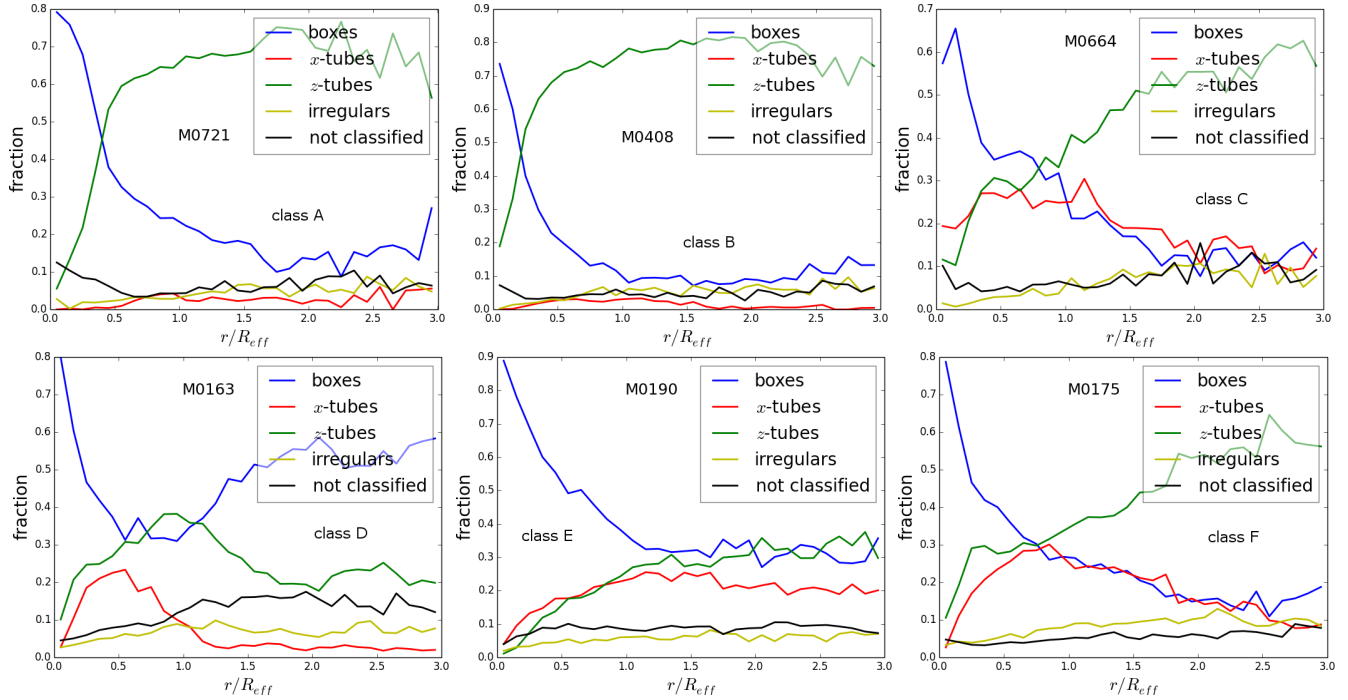


Figure 7. Fraction of box (blue), x -tube (red), z -tube (green), irregular (light green) and not classified (black) orbits as a function of radius for six galaxies with different formation histories (Naab et al. 2013). All simulated galaxies are dominated by box orbits at the center (which probably is an artifact of the simulation model we use). Galaxies of classes A and B become z -tube dominated at $\sim 0.5R_{\text{eff}}$, x -tubes can be found for classes C, D, E, and F. Typically less than 10 per cent of all orbits are irregular or not classified.

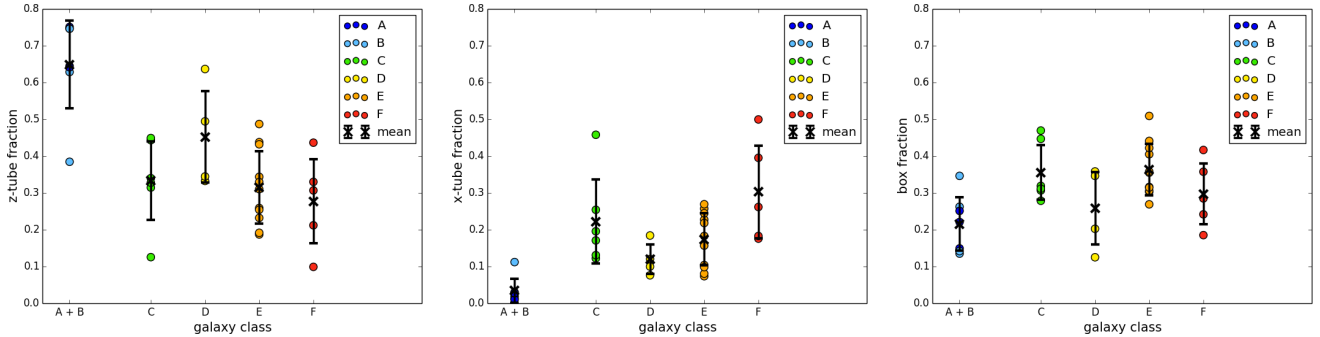


Figure 8. Fraction of z -tubes (left), x -tubes (middle), and box orbits (right) in the radial range of $0.5R_{\text{eff}}$ to $1.5R_{\text{eff}}$ (smaller radii are dominated by box orbits—which probably is an artefact of the simulation model we use) for different assembly classes as defined in Naab et al. (2013). For the individual classes we also show the mean fractions with their standard deviation as error bars. Fast rotators (classes A, B, and D) have high z -tube fractions, slow rotators (C, E, and F) have significant x -tube and box orbit contributions.

z -tube component (equally important co- and counter-rotating populations, see Fig. 14) with a relatively high line-of-sight velocity dispersion (peaking at about 280 km/s at $\sim 0.5R_{\text{eff}}$ with a drop in the center, see also Fig. 14). Also the z -tubes show a characteristic box shape, i.e. they are not as flat as the one shown in Fig. 4, but rather ‘opened’ in the edge-on projection (which is a typical behavior for tubes in non-axisymmetric potentials, see also Jesseit et al. 2005). Again, the nuclear dispersion is driven by the (very flattened) box orbit population. The system has a significant x -tube population (20.2%) contributing to the dispersion around one R_{eff} .

We have one simulated galaxy (M0094) with a counter-rotating core. For which we show the line-of-sight kinematics for the different orbit classes separated into prograde and

retrograde z -tubes, boxes and x -tubes. In the global line-of-sight velocity map (upper left panel of Fig. 13) the counter-rotating core ($r \lesssim 0.3R_{\text{eff}} \simeq 2.2$ kpc) is visible enclosed by the central isodensity contour. The left part of the nucleus has a negative velocity (light blue) of ~ -50 km/s and a positive velocity at the opposite side. At larger radii the velocities change sign. Again, the z -tubes alone carry a moderate amount of global rotation but the counter rotating core becomes clearly visible (middle left panel of Fig. 13). It is not a distinct subsystem but generated by two extended counter-rotating z -tube components. The center is dominated by retrograde z -tubes—the counter rotating core—larger radii ($r \gtrsim 0.5R_{\text{eff}}$) become dominated by prograde z -tubes (see Fig. 10). Overall, however, the system is dominated by box orbits ($\sim 42\%$ of the stars are on box orbits). The character-

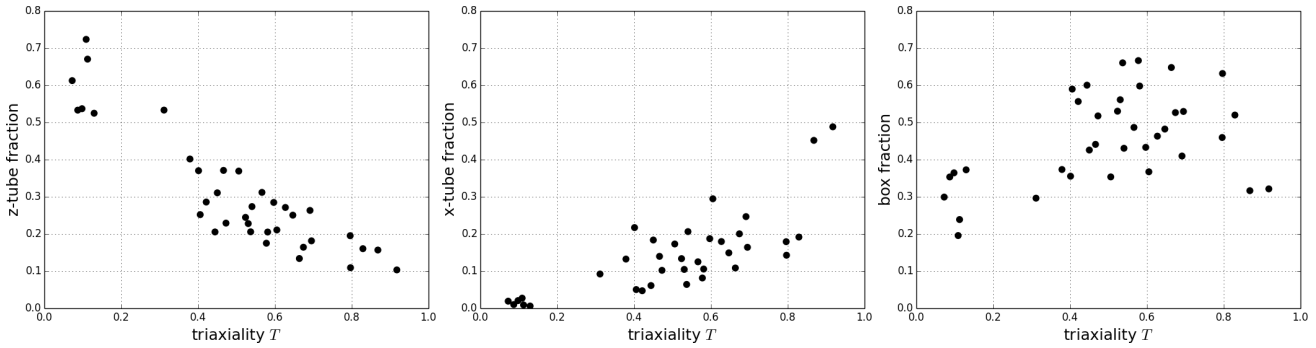


Figure 9. The total fraction of stars on z -tubes (left panel), x -tubes (middle panel), and box orbits (right panel) as a function of galaxy stellar triaxiality T (both measured within R_{eff}). Oblate systems ($T = 0$) are z -tube dominated, prolate systems ($T = 1$) can support x -tubes, and triaxial systems ($T = 0.5$) have the highest box orbit fraction as predicted by theory (Statler 1987) found for binary merger remnants (Jesseit et al. 2005).

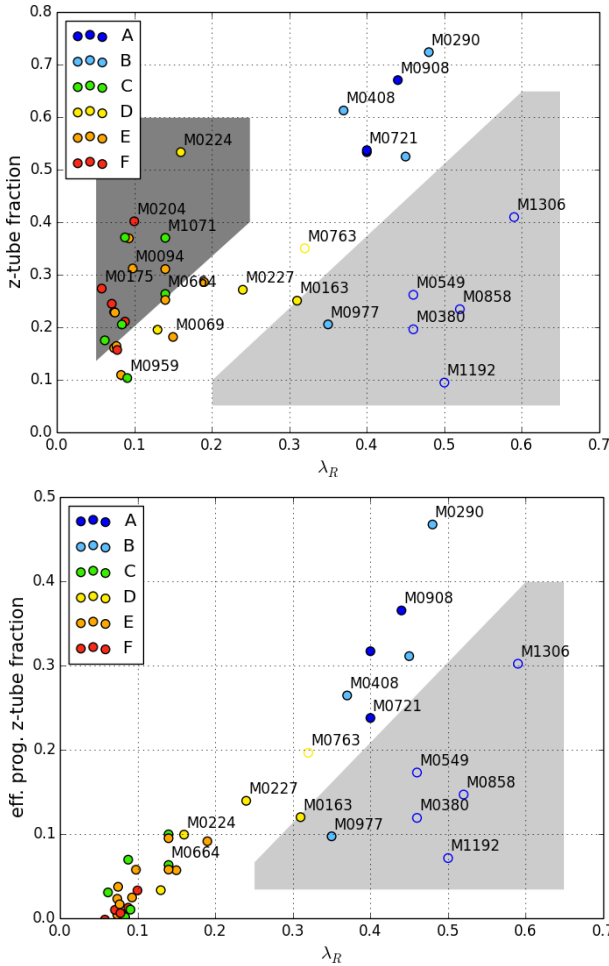


Figure 14. *Upper panel:* The z -tube fraction (within R_{eff}) of the simulated galaxies versus the λ_R -parameter. There is no correlation. Many low angular momentum galaxies have high z -tube fractions (dark grey shaded area) and high angular momentum systems can have low z -tube fractions (light grey shaded area). *Bottom panel:* The effective prograde z -tube fraction correlates nicely with λ_R for most of the galaxies. The galaxies below the linear correlation (in the light-grey shaded triangle) are roughly those, for which we find signs of significant figure rotation (unfilled circles).

istics of this simulated counter-rotating core resembles the only observed and modeled system with a counter-rotating core, NGC 4365 (van den Bosch et al. 2008). This system, however, is dominated by tube orbits and the core is more clearly visible.

In the upper panel of Fig. 14 the (global) z -tube fraction of the galaxies is plotted against their λ_R -parameter. Surprisingly, there is almost no correlation. In particular, galaxies with low λ_R can have z -tube fractions as high as 0.5. As mentioned before, the global rotation of a galaxy can be low if the angular momentum on prograde and retrograde z -tubes cancels out. This is the case for galaxies with low λ_R in the dark grey region in Fig. 14, mostly slow rotators of classes C, D, E and F.

A better measure for the amount of streaming motion is the ‘effective prograde z -tube fraction’, which we define as the normalized difference of the fraction of prograde and retrograde z -tubes:

$$\frac{(\# \text{ prog. } z\text{-tubes}) - (\# \text{ retrog. } z\text{-tubes})}{\# \text{ all orbits}}. \quad (10)$$

Plotting this fraction against λ_R (lower panel of Fig. 14) brings down the galaxies from the dark grey area onto a tight correlation with λ_R for most galaxies. This indicates that for most simulated galaxies the z -tube orbit family (and their separation into prograde and retrograde orbits) determines the global rotation properties of the galaxies.

Galaxies, which do not follow the correlation of λ_R and the effective prograde z -tube fraction (those in the light-grey area in Fig. 14) are mostly of galaxy class A (fast-rotators with gas-rich minor mergers) and are also those, for which we found clear signs of figure rotation (indicated by open circles in Fig. 14). Although the orbit classification for those galaxies is uncertain, we strongly suspect that the high λ_R values have a significant contribution from figure rotation. The non-rotating galaxies for which we trust our classification, the effective prograde z -tube fraction correlates nicely with the λ_R -parameter.

4.3 Orbits and LOSVD asymmetries

For most observed fast rotating galaxies the amplitude of the third-order component (h_3) of a Gauss-Hermite fit to the line-of-sight velocity profile (Eq. 7) anti-correlates with

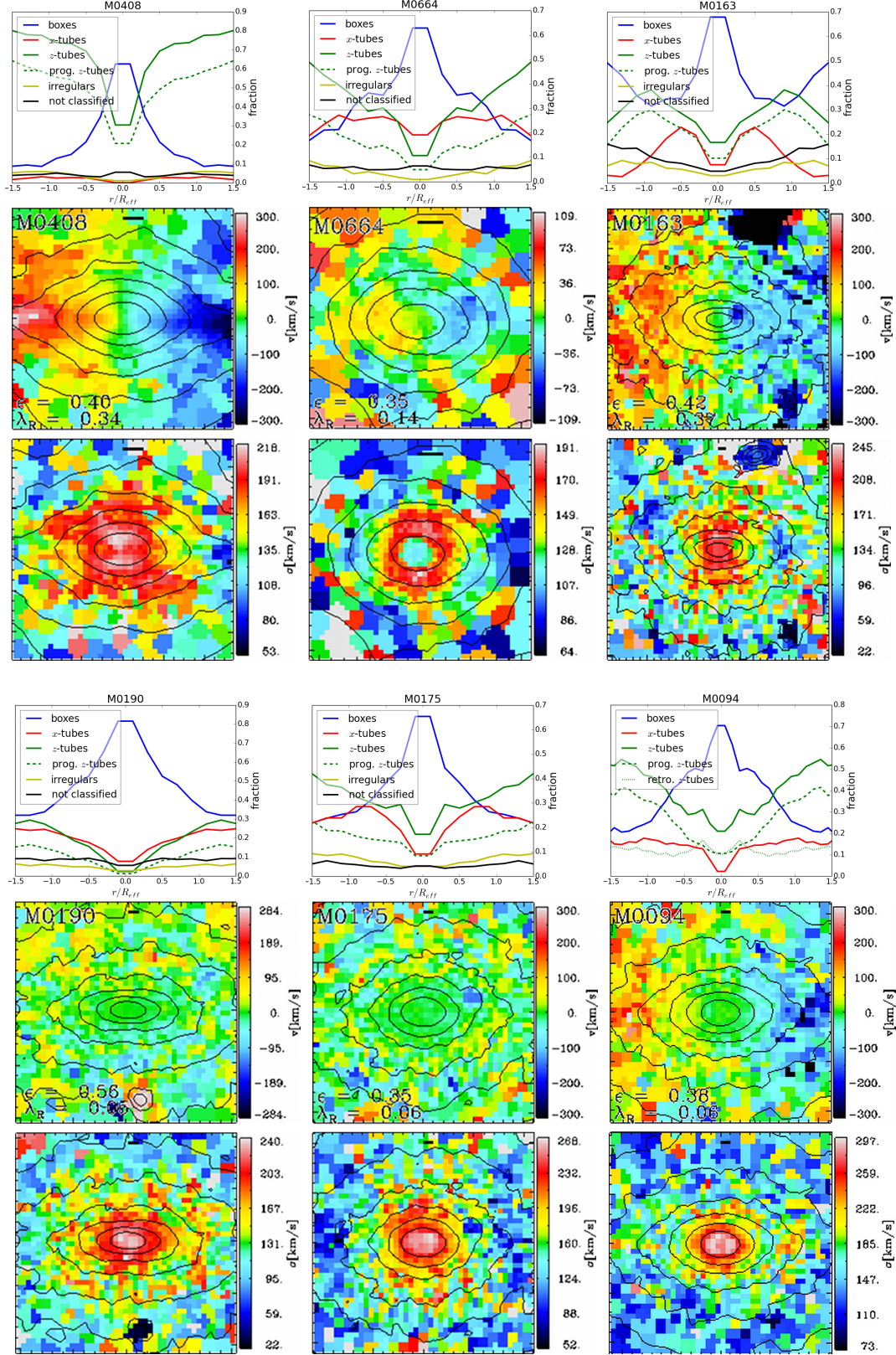


Figure 10. Two-dimensional line-of-sight velocity and velocity dispersion maps with isodensity contours for the six prototypical galaxies within $1.5 R_{\text{eff}}$. The λ_R parameter and the isophotal ellipticity at R_{eff} is given in the line-of-sight velocity panels. The black bar indicates 1 kpc. For comparison we show the radial orbit fractions (Fig. 7) mirrored at $r = 0$. Galaxies with fastest rotation (M0408 and M0163), have the highest prograde z-tube fractions with relatively few canceling retrograde z-tubes. If the latter is not the case, high z-tube fractions do not yield strong rotation (M0664 and M0175). M0094 has a counter-rotating core, where we see both: at the core the retrograde z-tubes (slightly) dominate and at larger radii the prograde z-tubes (clearly) dominate.

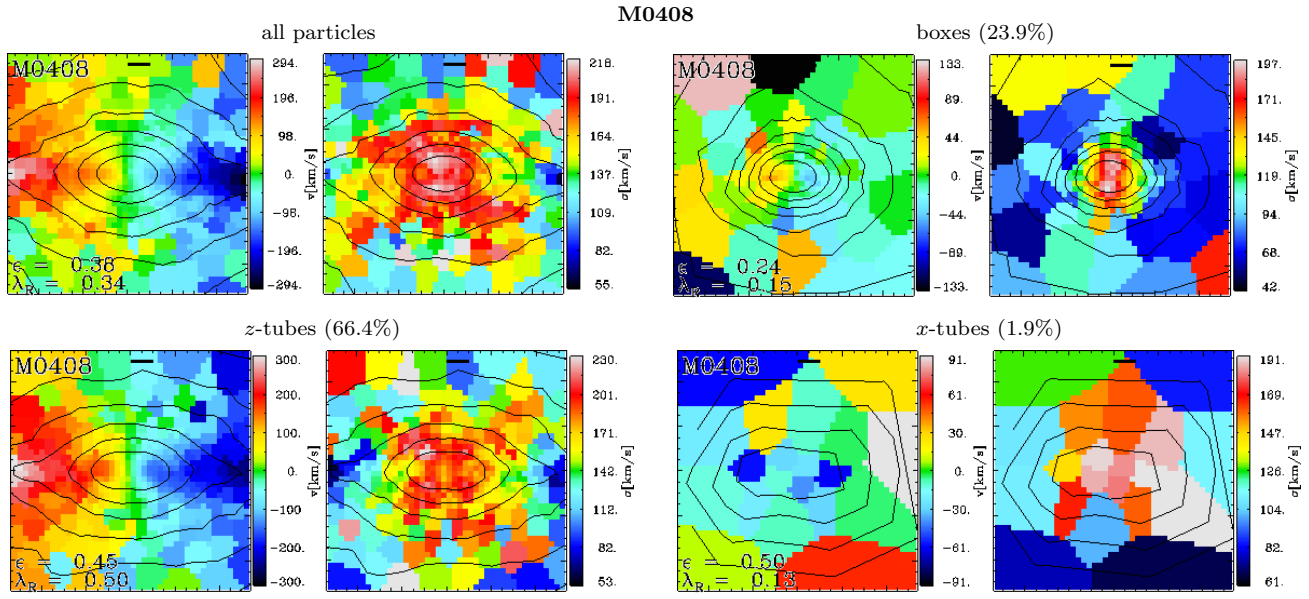


Figure 11. The line-of-sight velocity and velocity dispersion maps with isodensity contours of all star particles of M0408 up to $1.5 R_{\text{eff}}$ (top left), for all stars on box orbits ($\sim 24\%$, top right), stars on z -tubes ($\sim 66\%$, bottom left) and x -tubes ($\sim 2\%$, bottom right). The given orbit fractions are for stars in the maps and can differ from the values those given in Tab. 2. The rotation (see also the respective λ_R values) and the flattening originates z -tubes. The high dispersion at the center is supported by box orbits.

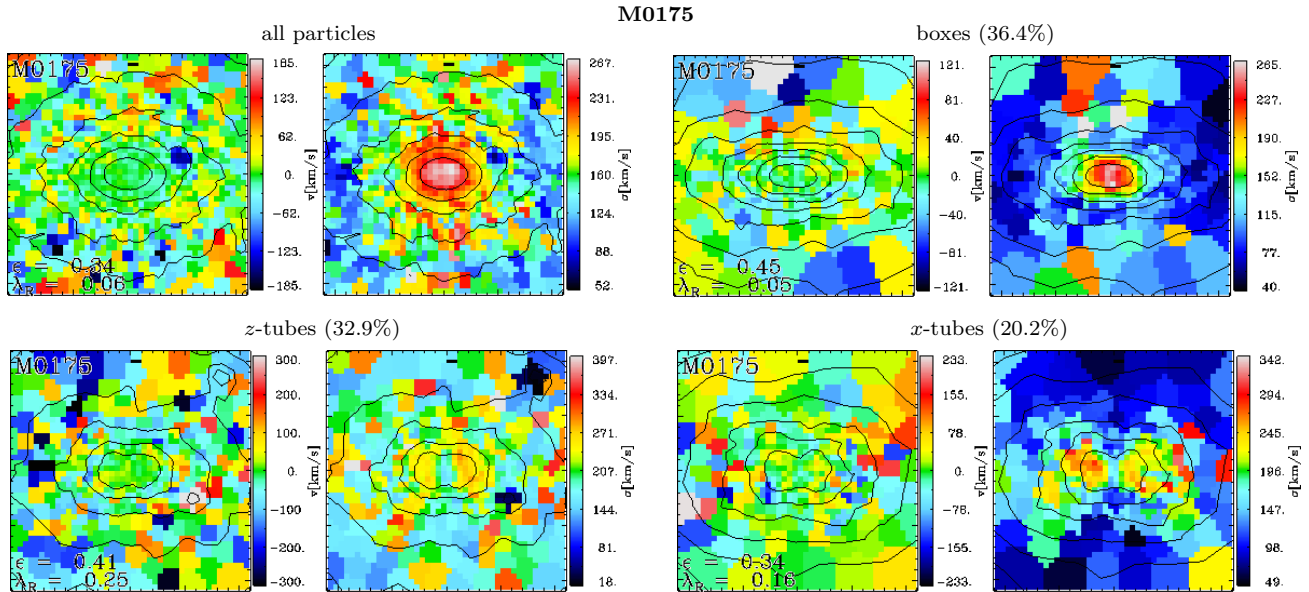


Figure 12. The line-of-sight velocity and velocity dispersion maps of M0175 and its orbital components like for M0408 in Fig. 11. The particles on z -tubes (lower left panel) are distributed equally on prograde and retrograde orbits resulting in low net rotation ($\lambda_R \sim 0.25$). The high dispersion inner part of the system is determined by the properties of box orbits (upper right panel). The system has a significant x -tube population contributing to the dispersion at $\sim 1 R_{\text{eff}}$.

rotational support (V_0/σ ; Bender et al. 1994; Halliday et al. 2001; Pinkney et al. 2003; Krajnović et al. 2013; for the V_0/σ data from the ATLAS^{3D} sample see Krajnović et al. 2011, 2008). The velocity profile has a steep leading and a long trailing wing. This holds for oblate systems resembling tow-integral models (Dehnen & Gerhard 1994; Bender et al. 1994) and/or can be indicative of an embedded disk component (van der Marel & Franx 1993; Bender et al. 1994; Fisher 1997; Naab & Burkert 2001; Krajnović et al. 2013). In this section we use the cosmological galaxy formation

simulations to explain the origin of the anti-correlation of h_3 and V_0 and its connection to the orbital structure.

Naab et al. (2013) found that only fast rotating galaxies with late gas-rich mergers or late dissipation (classes A and B in their classification) show a h_3 - V_0/σ anti-correlation. These are also the galaxies with the highest λ_R -parameter and, as we have shown here, those with a the highest effective prograde z -tube fraction.

It has been shown with idealized experiments that gas dissipation (cooling gas flow to the center, triggered by

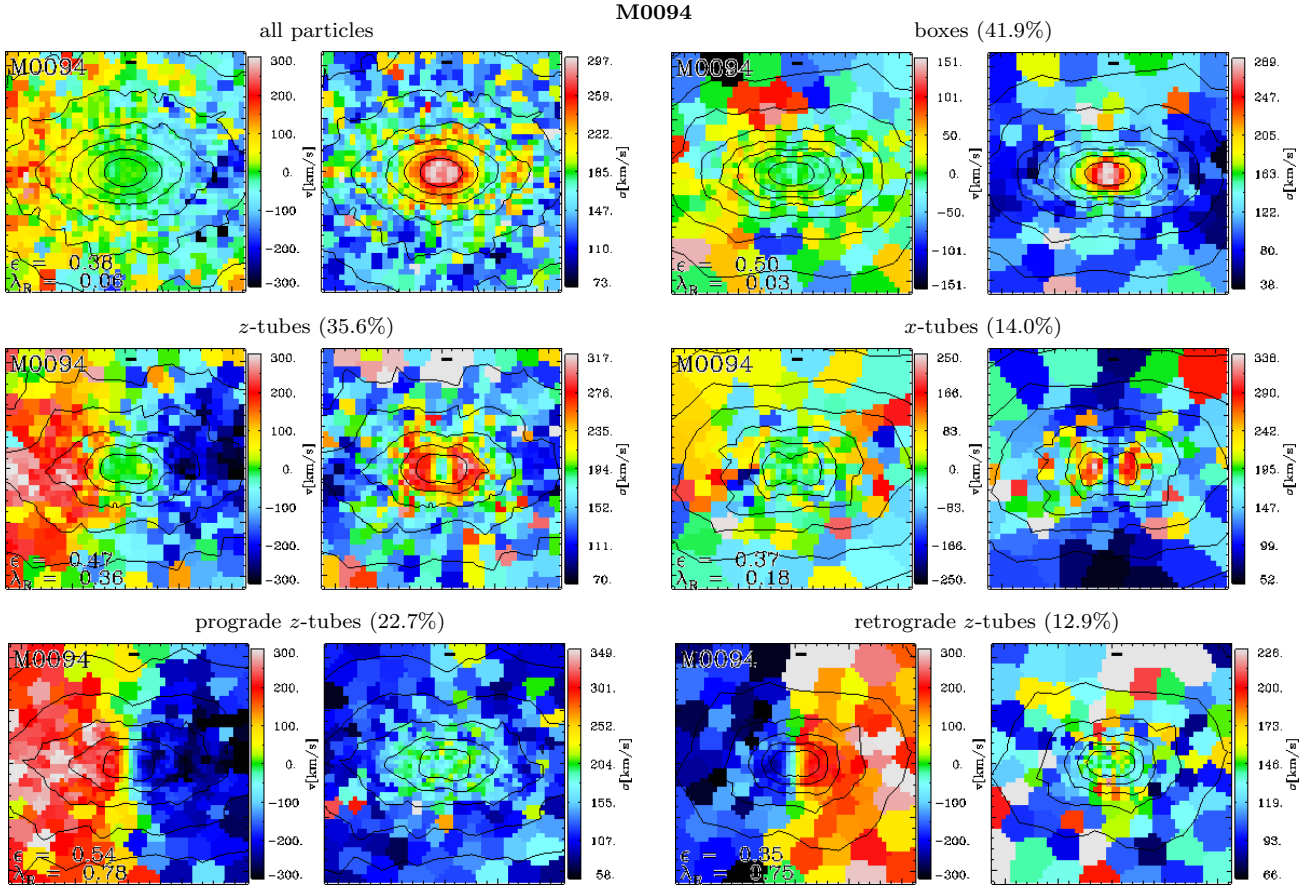


Figure 13. The line-of-sight velocity and velocity dispersion maps of M0094 (galaxy class E) and its orbital components like for M0408 in Fig. 11. The galaxy has a counter-rotating core visible in the line-of-sight velocity (upper left panel) which is generated by the z -tube population (middle left panel) consisting of prograde and retrograde orbits (bottom panels). The overall kinematics of the system is determined by the dominant non-rotating box orbit population (upper right). This galaxy also has a sizable x -tube component (12.9%).

a merger event) can explain this behavior. In collisionless mergers the stellar population of the remnant is dominated by stars on box orbits and even if the remnant is rotating the LOSVD has steep trailing wing (positive h_3) which is hardly observed (Naab & Burkert 2001). Gas inflow during a merger, however, leads to centrally concentrated, axisymmetric potentials, suppressing the population of box orbits (Barnes & Hernquist 1996). With now more stars on z -tubes (which carry the angular momentum) the LOSVD gets a steep leading wing and the observed anti-correlation of h_3 and V_0/σ can be recovered (Naab et al. 2006). This is supported by the formation of new stars in a re-forming disk (Naab et al. 2006; Hoffman et al. 2009, 2010 and also see Bender et al. 1994).

Here we present the same effect for two galaxies formed in a cosmological context. In the top panels of Fig. 15) we show the two-dimensional maps of $V_0, \sigma, V_0/\sigma$, and h_3 for M0277, a fast rotating galaxy that has experienced a late gas-poor (collisionless) major merger (typical for the class D galaxies in Naab et al. 2013). For this galaxy the LOS velocity and h_3 are correlated. In the bottom panel of Fig. 15 we show, as an example, the LOSVD at $\sim 0.6R_{\text{eff}}$. It is dominated by non-rotating stars (73%) without net-rotation—mostly on box orbits. The stars on prograde z -tubes shift the peak towards positive velocities. The resulting distribution is almost symmetric as not only the prograde z -tubes

(not as dominant as the box orbits) broaden the distribution towards positive values, but there are also some retrograde z -tubes, that do the same towards negative velocities. Hence, only a slightly positive value for h_3 .

For M0408 the situation is different. This galaxy is a fast rotator with late gas-rich major merger and it shows a clear anti-correlation of the LOS velocity and h_3 (top panels Fig. 16). A typical LOSVD is shown in the bottom panel of Fig. 16. At the same radius this galaxy is dominated by high angular momentum z -tube orbits which by themselves already generate a LOSVD with a steep leading wing. The broad trailing wing hosts stars on retrograde tubes. Stars on other orbits without angular momentum do not affect the shape of the LOSVD very much.

If we restrict ourselves to galaxies without figure rotation, we can conclude that all orbits apart from z -tubes have no intrinsic angular momentum (around the minor axis) and hence their LOS velocity profile is almost symmetric and peaks around $v = 0$. The z -tube orbits can be approximated as two peaks: one from retrograde and one from prograde z -tubes. For a rotating system (around the minor axis) the latter peak has a larger amplitude. If the other orbits (centering at $v = 0$) are subdominant (like in Fig. 16) the overall distribution then peaks with the prograde z -tubes has a trailing wing that is broadened by the retrograde z -tubes and other orbits. If the other orbits, however, are dominant

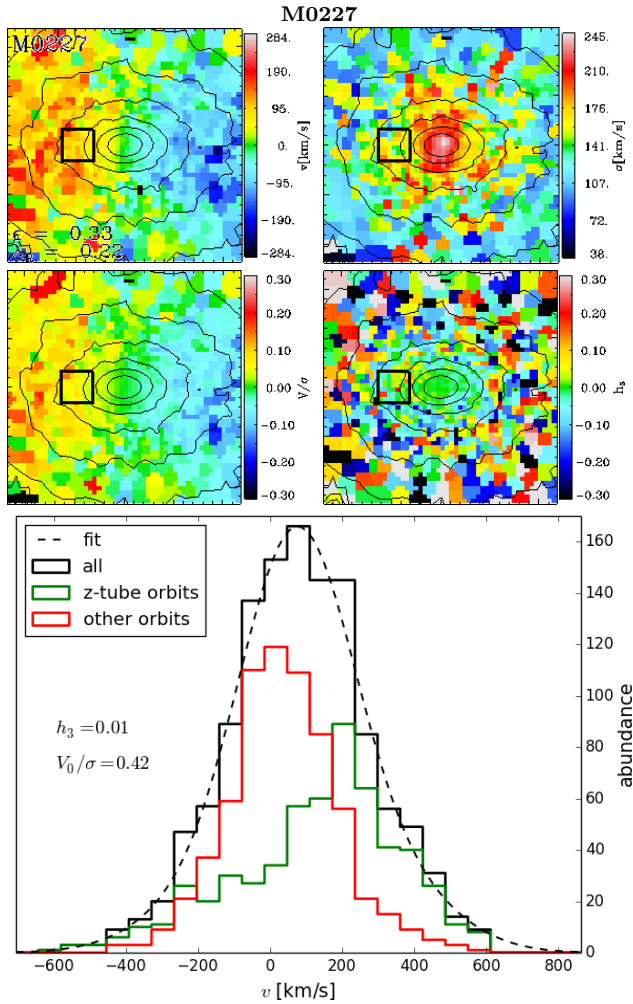


Figure 15. Characteristic line-of-sight velocity distribution for all stellar particles (bottom panel, black histogram) at the major axis around $0.6R_{\text{eff}}$ ($0.4R_{\text{eff}} < x < 0.8R_{\text{eff}}$ and $-0.2R_{\text{eff}} < z < 0.2R_{\text{eff}}$) for the fast rotating galaxy M0227 (class D). The investigated region is indicated in the line-of-sight velocity, dispersion, V_0/σ and h_3 maps (top panels) as black squares. The black dashed line indicates the Gauss-Hermite fit to the LOSVD with $h_3 = 0.01$. The LOSVD of stars on z -tube orbits (green histogram) peaks at $v \approx 200$ km/s, but the total LOSVD is dominated by particles which are mostly on box orbits (red histogram) peaking at $v \approx 0$. Such a profile is typical for fast rotating galaxies formed in dissipationless mergers (Naab & Burkert 2001; Naab et al. 2006, 2013).

(like in Fig. 15), the overall distribution peaks in-between the prograde z -tubes and the other orbits and is rather symmetric.

4.4 Signatures of two phase assembly

All galaxies presented here consist of two populations of stars. One has formed within the galaxy (the *in situ* component) and the second has formed in other galaxies and have been accreted in mergers (the accreted component). In general, *in situ* formation dominates at high redshift and the accretion of stars becomes more important at low redshift, and more so for massive systems (Guo & White 2008; Oser

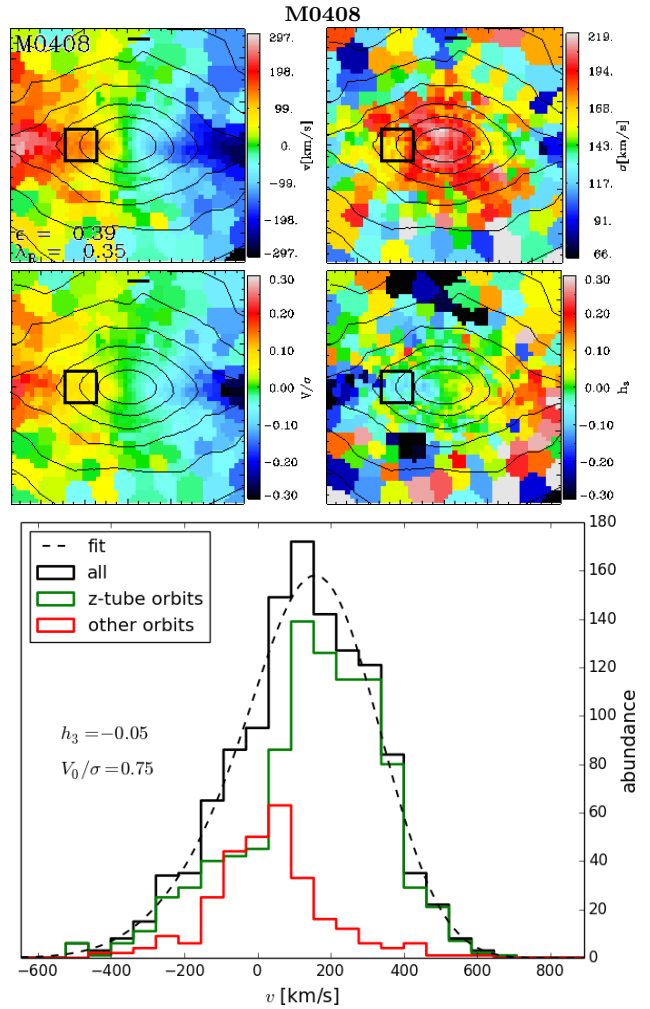


Figure 16. Same as Fig. 15 but for the fast rotating galaxy M0408 (Class B). Here the stellar orbits in the observed region are dominated by tubes (green histogram) generating an overall LOSVD with a steep leading wing (black histogram and dashed line, $h_3 = -0.05$). Other orbit classes (red histogram) are sub-dominant. Typically high tube-to-box fractions generate LOSVDs with steep leading wings (Naab et al. 2006; Hoffman et al. 2010) and such a LOSVD is typical for fast rotating galaxies that have formed under the significant influence of dissipation (see e.g. class A and B in Naab et al. 2013).

et al. 2010; Lackner et al. 2012; Moster et al. 2013; Naab 2013). The separate origin of these components might also results in different orbit populations.

In Fig. 17 we plot the orbit fractions of the *in situ* and accreted component as well as for the dark matter particles as a function of radius for four characteristic examples. Surprisingly, most galaxies show little difference in the orbital composition of these components (M0163 and M0175). Possible small difference might be washed out, since for individual particles the orbit classification is uncertain on the per-cent level (see Sec. 3.4). For M0664 and M0917, however, the orbit composition of the *in situ* component is clearly distinct.

The former has a tube biased *in situ* component and has a recent gas-poor major merger, where the different dynamical history of the two merged galaxies is still imprinted in the

orbit structure. The latter, M0977, had a late gas-rich major merger, in which new stars formed the dissipative component, and thus it has a prominent late *in situ* formed component that is populating mostly z -tubes (except for the inner radii, $r \lesssim 0.5R_{\text{eff}}$). The orbital structure of the dark matter component, however, is always very similar to the accreted component, independent of the different assembly histories of the galaxies. It is plausible to assume that frequent mergers, which are relevant for galaxy classes C, D, E, & F, mix the *in situ* and accreted stellar populations efficiently and the dark matter particles behave in a similar way.

In addition the orbit analysis might not be the best diagnostics. Although z -tubes are all centrophobic they can significantly differ in shape from circular to very eccentric. A good measure for this behavior is provided by the anisotropy β (Binney & Tremaine 2008):

$$\beta \equiv 1 - \frac{\langle v_\phi^2 \rangle + \langle v_\theta^2 \rangle}{2 \langle v_r^2 \rangle}, \quad (11)$$

where v_r , v_ϕ , and v_θ are the velocities in spherical coordinates. This parameter is zero for isotropic motion, positive if the velocities are radial biased and negative if they are tangentially biased.

We plot the corresponding radial anisotropy profiles of M0163, M0175, M0664, and M0977 in the right panels of Fig. 17 and also separate the *in situ* component and accreted component as well as the dark matter particles. For M0664 and M0977 the orbital structure is reflected in the anisotropy profiles: where in galaxy M0664 the *in situ* stars populate box orbits more than the accreted stars do, there the motion of the *in situ* stars is also more radially biased than of the accreted stars; similarly for M0408, where the *in situ* stars are more tangentially biased, they preferentially populate z -tubes. However, we also see different anisotropy profiles for *in situ* and accreted stars in galaxies which show no significant difference in the orbit profiles, e.g. for M0175. Here the accreted stars are moderately radially biased ($\beta \approx 0.4$) whereas the *in situ* stars—having almost identical orbital structure—are isotropic. But this is not true for all galaxies. There are some that have alike β -profiles for *in situ* and accreted stars (e.g. M0163).

We also investigated the dark matter anisotropy profiles (black lines in Fig. 17) and they turned out to be very isotropic or sometimes mildly radially biased (cf. M0977) where they have a tendency to follow the accreted component. To see whether this is universal and to identify trends in the anisotropies, we plotted the β -profiles of the different galaxy classes (except for those galaxies that show a massive near-by substructure that would compromise the results) in Fig. 18. The dark matter particles are indeed always isotropic to mildly radially biased, with no trend along the different galaxy classes. The profiles of the other components, however, have clear dependencies on the assembly history of the galaxies.

We find the *in situ* component to have smaller β than the accreted component in general and in agreement with Wu et al. (2014), who grouped the galaxies among their *in situ* fractions and plotted the overall stellar anisotropy profiles for all galaxies. This is not surprising, since *in situ* stars form from the dissipative gas component, that settles down onto a rotating disk conserving angular momentum. The ro-

tating dynamical element is also imprinted in the *in situ* stars that then should preferentially populate z -tubes—the only ones with intrinsic rotation. The accreted star component has fallen in from all directions and, hence, are expected to be on more radially biased orbits.

We furthermore find that fast-rotators with late gas-rich mergers (classes A and B) have very tangentially anisotropic *in situ* components, especially beyond the effective radius. Accreted stars, however, are a bit radially biased and hence the overall stellar anisotropy is slightly radially biased for class A galaxies—those with late gas-rich minor mergers—anyway. Class B galaxies—those with late gas-rich major mergers—have similar anisotropies of the accreted stars, the *in situ* component, however, is even stronger tangentially biased than it is for class A galaxies. The importance of the *in situ* stars yields a tangentially biased stellar anisotropy.

Interestingly, the *in situ* stars are always slightly radially biased or isotropic at most for fast-rotators with late gas-poor major mergers (class D). Slow-rotators with gas-rich major mergers (class C) have very similar stellar anisotropy profiles. The *in situ* star, however, are mildly tangentially biased at large radii in contrast to those galaxies with gas-poor major mergers (classes D and E). We, hence, see that the gas fraction plays an about equally important role in determining the anisotropy of the *in situ* stars and we consequently find the most radially biased motion of the stars in slow-rotators with gas-poor major/minor mergers (classes E and F). For those with major mergers (class E) even the *in situ* stars are no longer tangentially biased and they are roughly isotropic for those with minor mergers.

It seems as the anisotropy parameter β is better correlated with the *in situ* fractions and the quantized nature of orbit classification can often not capture the different assembly histories of *in situ* and accreted stars. Moreover, β is better observable, and although the most prominent trends are at large radii ($r \gtrsim R_{\text{eff}}$), the differentiation between fast-rotators with gas-rich merger histories (classes A and B) and the other galaxy classes is already strong at smaller radii (compare yellow lines for stellar β in Fig. 18).

We see that the anisotropy indeed reveals more about the assembly history of the galaxies than the orbit classes do, but they also complement one another as the rotation of the galaxies is not directly reflected in the anisotropy profiles. The dark matter particles have very similar orbital structures as the stellar component (see Fig. 17), but they are very isotropic for all galaxies among our ensemble as it can be seen from Fig. 18. The anisotropies we find are also consistent with observational results: there is a relatively large variety of anisotropies (Thomas et al. 2007) but mostly mildly radially biased ones (de Lorenzi et al. 2008; Das et al. 2011) the only strong exception is fast-rotating galaxies with late gas-rich major mergers (class B) beyond the effective radius.

We plot the global fraction of stars that formed *in situ* since $z \approx 2$ against the anisotropy β in Fig. 19. *In situ* stars that have formed earlier have undergone multiple merger events and, hence, the fingerprint of their dynamical history in the anisotropy is probably washed out. We indeed see a weak correlation, though only for the inner parts ($r \lesssim 0.5R_{\text{eff}}$) of the galaxies (Fig. 19). For the region $0.5R_{\text{eff}} < r < 1.0R_{\text{eff}}$ there is already very little correlation left. This is mainly due to the fact that the *in situ* fractions in this

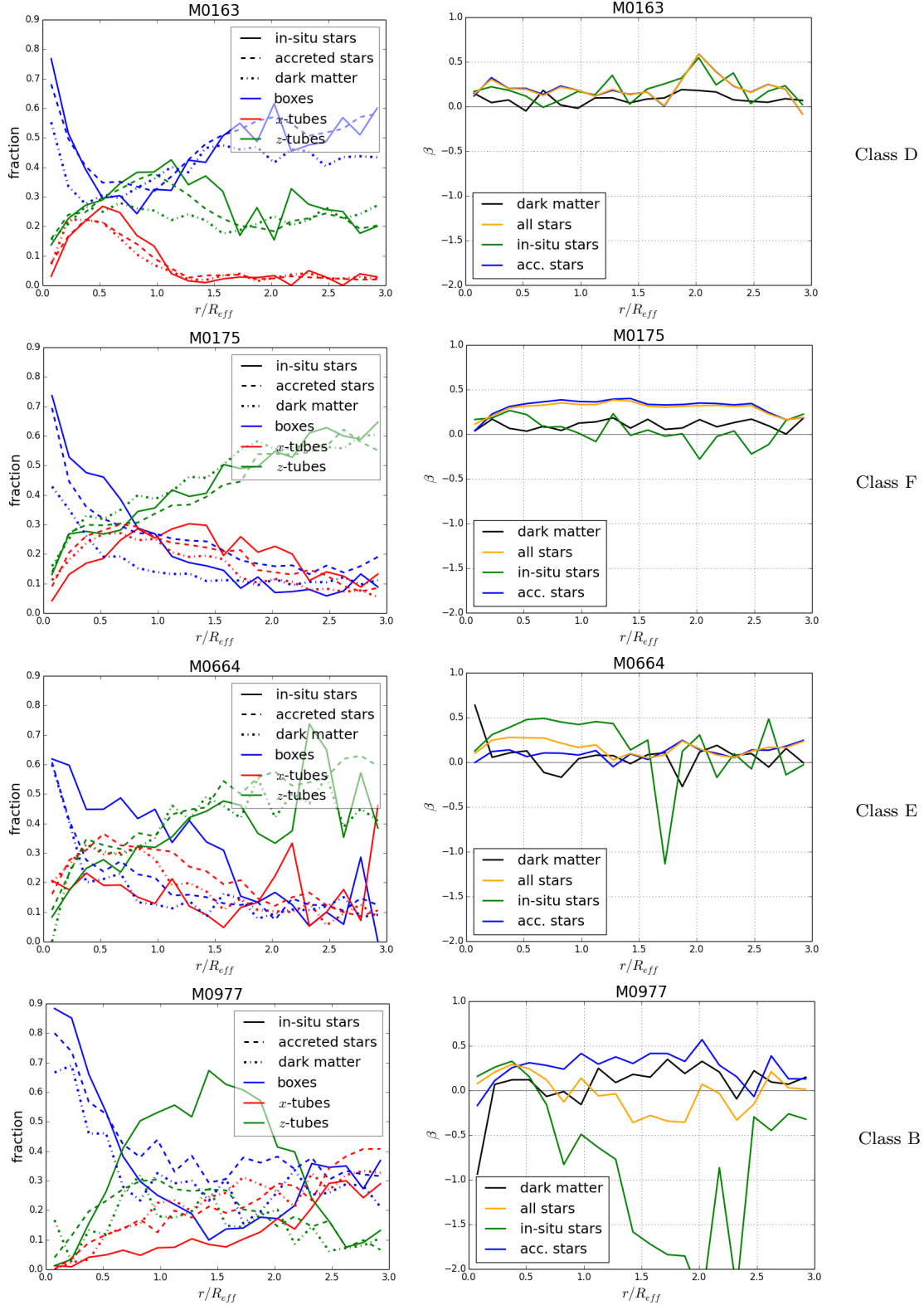


Figure 17. Left panels: The radial orbital structure of the *in situ* stars (solid lines) and the accreted stars (dashed lines) as well as dark matter particles (dash-dotted lines) for four galaxies (M0163, M0175, M0664, and M0977). For most galaxies with collisionless recent assembly histories (classes D, E, and F) there is almost no difference between the *in situ* and accreted component and the dark matter particles. If there are mild variations (like for the box population in M0664) the accreted stars and dark matter are more alike. This is also true for M0977, but this galaxy has relevant late *in situ* star formation (and no late large mergers) forming a prominent z-tube population dominating most of the galaxy. Right panels: The anisotropy parameter β as a function of radius for dark matter (black), all stars (yellow), as well as separated into the *in situ* (green) and accreted (blue) component. The dark matter is in general isotropic at all radii. M0163 is dominated by box orbits at all large radii and radially biased ($\beta \sim 0.2$). M0175 is dominated by z-tubes at large radii but here the *in situ* stars are more isotropic than the accreted stars which are also on z-tubes but clearly radially biased. For M0977 this effect is even stronger with a clearly tangentially biased *in situ* component.

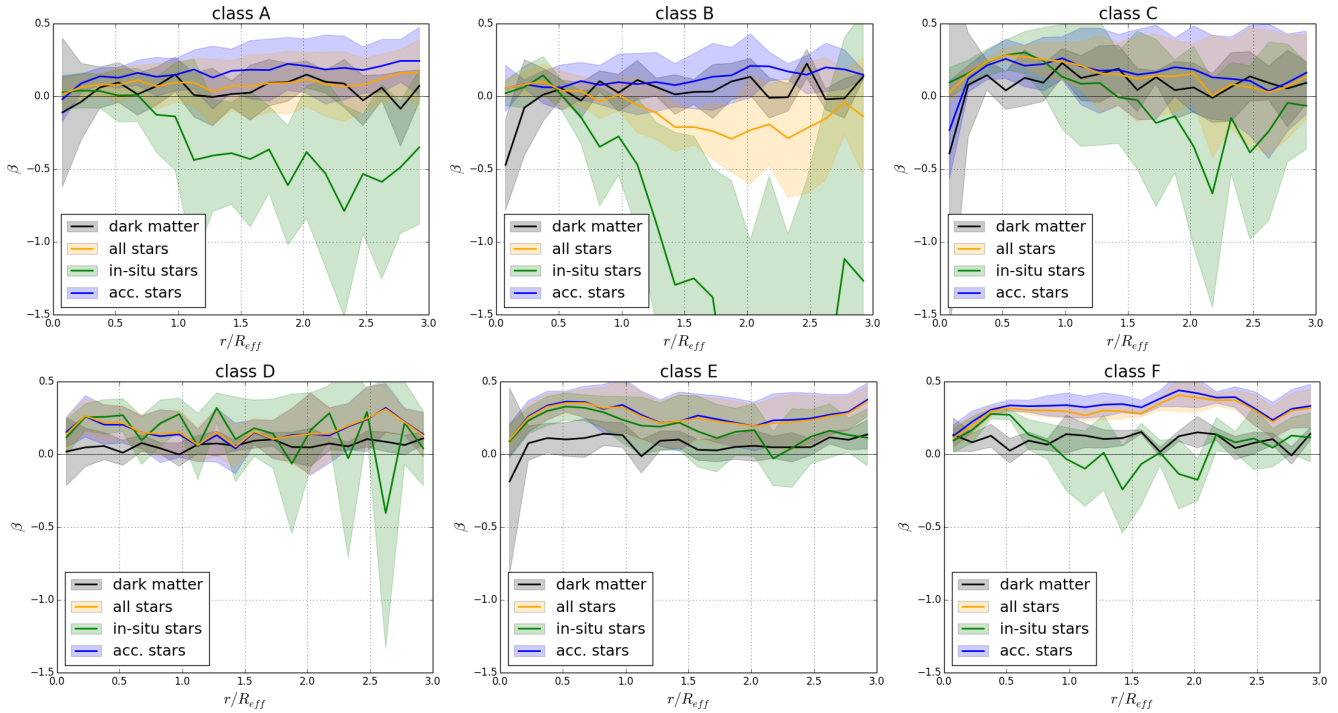


Figure 18. The mean anisotropy parameter profile (line) for dark matter and stars as well for the *in situ* and accreted components only is plotted for the different galaxy classes. Three galaxies—M0069 (E), M0162 (E) and M0948 (F)—that have heavy nearby substructures (indicating an on-going/up-coming major merger) are excluded from these calculations. The pale bands around the mean indicate the standard deviation among the galaxy classes.

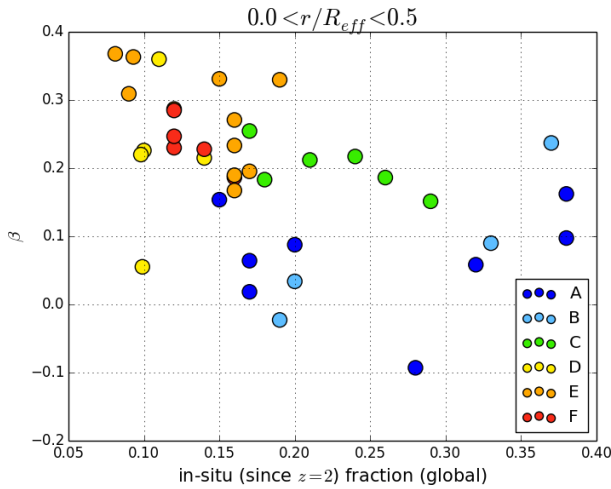


Figure 19. For the inner part of the galaxies ($r < 0.5 R_{\text{eff}}$, upper panel) the anisotropy parameter β correlates with the *in situ* fraction. Furthermore, the galaxy classes from Naab et al. (2013) separate in the diagram. For larger radii, however, the correlation is nearly completely gone (see lower panel).

region has decreased by a factor of almost two from that within $0.5 R_{\text{eff}}$, and hence they do not influence β as much.

Moreover, we see that the galaxy classes defined by Naab et al. (2013) separate in the anisotropy–*in situ* fraction diagram. Fast-rotators with late gas-rich mergers or late dissipation (classes A and B) have rather high *in situ* fraction and are isotropic or slightly tangentially biased. Slow-rotators with late gas-rich major mergers (class C) still have

high *in situ* fractions due to the shocking gas in the mergers, but are more radially biased, since they do not rotate as much. The remaining classes of fast-rotators with late gas-poor major mergers (class D) and slow-rotators with gas-poor mergers (classes E and F) are located in the upper left corner in the diagram with small *in situ* fractions and are tangentially biased.

5 SUMMARY AND DISCUSSION

We have presented an orbit analysis of star and dark matter particles out to three effective radii for a sample of 42 galaxies formed in cosmological zoom simulations of Oser et al. (2010). With an improved version of the Carpintero & Aguilar (1998) spectral classification scheme we classified orbits of stars and dark collisionless dark matter particles. For the stellar orbits we found that box orbits and z -tubes are most abundant among the simulated galaxies. The distribution of orbits with radius, however, can vary significantly from galaxy to galaxy. A common feature is the relatively high central ($r \lesssim 0.4 R_{\text{eff}}$) box orbit fraction, much higher than what is found when triaxial Schwarzschild models are applied to observed LOSV maps (c.f. NGC 4365, van den Bosch et al. 2008 and NGC 3379 and NGC 821, Weijmans et al. 2009). It is likely that underestimating the influence of dissipation of the assumed model (see the discussion in Oser et al. 2010) and/or neglecting black hole impact play a significant role. Both (not included) effects will help to make the central region more axisymmetric and therefore suppress the population of box orbits.

Galaxies with figure rotation (6 out of 42), which have

uncertain orbit fractions, were identified and we excluded them from any interpretation that uses orbit analysis. For the remaining galaxies we show that LOS rotation, quantified by the λ_R -parameter, originates from streaming motions of stars. We demonstrate that the value of λ_R directly correlates with the ‘effective prograde z -tube fraction’ (i.e. the difference of the fraction of prograde z -tubes and the fraction of retrograde z -tubes normalized by the total number of z -tubes).

We find the expected correlations of box orbit, z -tube, and x -tube fractions with galaxy triaxiality (e.g. Jesseit et al. 2005). z -tubes live in oblate systems, x -tubes in prolate ones and box orbits are most abundant in very triaxial systems ($T \approx 0.5$). We construct mock LOSV maps—also from single orbit families—of the simulated galaxies and recover the observational impact of the different orbit families. For example, rotation originates from streaming motion of stars on z -tubes as expected from the investigation of the correlation of the effective prograde z -tube fraction and the λ_R parameter. One galaxy has a counter-rotating core and, similar to NGC 4365, we are able to demonstrate that the core is not a kinematically decoupled system, but originates from a superposition of the smooth distributions of prograde and retrograde z -tubes (c.f. van den Bosch et al. 2008).

Using the orbit classification, we also can also explain the origin of the observed anti-correlation between h_3 and V_0/σ . Many simulated fast rotators show an anti-correlation but correlated h_3 and V_0/σ is also possible. The group of galaxies with enhanced dissipation, i.e. with more ‘late’ *in situ* star formation due to gas accretion or gas-rich mergers, shows a clear tendency for an anti-correlation (Naab et al. 2013). The increased relative fraction of prograde tube orbits creates a steep leading wing in the LOSVD. Physically, this originates from a suppression of box orbits in more axisymmetric potentials. Rotating systems with little late dissipation do not show this anti-correlation. This conclusion is in agreement with studies of isolated mergers (Naab et al. 2006; Hoffman et al. 2009, 2010).

Using the six galaxy classes with different formation histories defined in Naab et al. (2013) we only see weak trends of orbit fractions with the formation history apart from systems with late dissipation showing high z -tube fractions. Surprisingly, the distribution of orbits of the *in situ* formed stars, accreted stars, and dark matter particles are very similar, with the exception of galaxies with a lot of late dissipation. This result compares well with Bryan et al. (2012), who find similar distributions for stars and dark matter particles at larger radii. Only two of our galaxies exhibit a clear distinction between the orbit profiles of *in situ* formed and accreted stars. One system with a late gas-rich major merger (M0977) has a higher fraction of z -tubes for the *in situ* formed stars than for the accreted stars. This is expected as the *in situ* stars form from the dissipative gas component which can settle onto an axisymmetric, oblate disk before star formation. This is ‘memorized’ in the kinematic features and preferentially populates stars on z -tubes.

We found that the velocity anisotropy (measured by the β parameter) depends more on the formation history than orbit distribution. Galaxies with gas-rich mergers and gradual dissipation have can have mildly radially biased motions of the stars ($\beta \simeq 0.2$) and tangentially biased motions

of the stars (up to $\beta \simeq -0.5$), especially at larger radii ($r \gtrsim R_{\text{eff}}$). Galaxies with dry mergers always have radially biased motions of stars ($0.1 \lesssim \beta \lesssim 0.4$). Stars that form *in situ* from the dissipative gas component tend to have tangentially biased motions, whereas accreted stars fall in on radially biased trajectories and hence preferentially end up on tangentially biased orbits. We find that *in situ* formed stars are mildly radially anisotropic ($\beta \simeq 0.25$) for gas-poor major mergers remnants and otherwise isotropic to strong tangentially anisotropic ($\beta < -1.0$) for fast-rotators with gas-rich mergers. The dark matter particles, however, are always close to isotropic. Orbit families are less well correlated as for example tube orbits can become radially biased when they become eccentric.

It is plausible to assume that *in situ* stars and accreted stars can have different metallicities but the accreted galaxies have lower mass (e.g. Villumsen 1982; Hilz et al. 2013). Therefore it will be interesting to investigate a connection between metallicities and kinematic properties (orbit families, anisotropy, etc.). Zoom-simulations reproducing the observed evolution of the mass–metallicity relation (e.g. Hirschmann et al. 2013; Aumer et al. 2013) would be well suited for this. As our simulations do not follow metal evolution such an investigation is, however, beyond the scope of this paper. However, orbit families do provide important information about the formation processes. Both AGN feedback and stellar feedback can lead to a more or less dissipative formation of galaxies (see e.g. Mo et al. 1998; Hirschmann et al. 2012; Dubois et al. 2013; Übler et al. 2014). Enhanced dissipation results in more axisymmetric and oblate galaxies and with have higher z -tube fractions (the dissipative formation of disk galaxies is an extreme example, e.g. Aumer et al. 2013). For large radii Bryan et al. (2012) could indeed show that feedback rises the amount of z -tubes and reduced the amount of box orbits for star particles as well as dark matter particles. However, the impact of dissipation might be particularly important for galaxy centers. Furthermore, feedback can change merger histories (in general reduces the number of minor mergers) and increases gas accretion and the amount of gas involved in mergers (e.g. Hirschmann et al. 2012; Übler et al. 2014). Therefore ‘feedback physics’ might leave a clear fingerprint in the orbital composition of massive galaxies.

6 ACKNOWLEDGEMENTS

We thank Davor Krajnović for his comments and suggestions and thank the anonymous referee for valuable suggestions. Thorsten Naab acknowledges support by the DFG cluster of excellence ‘Origin and Structure of the Universe’.

REFERENCES

- Arnold J. A., Romanowsky A. J., Brodie J. P., Forbes D. A., Strader J., Spitler L. R., Foster C., Blom C., Kartha S. S., Pastorello N., Pota V., Usher C., Woodley K. A., 2014, *ApJ*, 791, 80
- Arnol'd V., 1989, *Mathematical Methods of Classical Mechanics*. Graduate Texts in Mathematics, Springer
- Arnol'd V. I., Kozlov V. V., Neishtadt A. I., 2007, *Mathematical Aspects of Classical and Celestial Mechanics*. Springer
- Aumer M., White S. D. M., Naab T., Scannapieco C., 2013, *MNRAS*, 434, 3142
- Bacon R., Copin Y., Monnet G., Miller B. W., Allington-Smith J. R., Bureau M., Carollo C. M., Davies R. L., Emsellem E., Kuntschner H., Peletier R. F., Verolme E. K., de Zeeuw P. T., 2001, *MNRAS*, 326, 23
- Bailin J., Steinmetz M., 2005, *ApJ*, 627, 647
- Barnes J. E., Hernquist L., 1996, *ApJ*, 471, 115
- Bender R., Saglia R. P., Gerhard O. E., 1994, *MNRAS*, 269, 785
- Binney J., Tremaine S., 2008, *Galactic Dynamics: Second Edition*. Princeton University Press
- Bryan S. E., Mao S., Kay S. T., Schaye J., Dalla Vecchia C., Booth C. M., 2012, *MNRAS*, 422, 1863
- Cappellari M., Copin Y., 2003, *MNRAS*, 342, 345
- Cappellari M., Emsellem E., Krajnović D. e. a., 2011, *MNRAS*, 413, 813
- Carpintero D. D., Aguilar L. A., 1998, *MNRAS*, 298, 1
- Clutton-Brock M., 1973, *Ap&SS*, 23, 55
- Das P., Gerhard O., Mendez R. H., Teodorescu A. M., de Lorenzi F., 2011, *MNRAS*, 415, 1244
- de Lorenzi F., Gerhard O., Saglia R. P., Sambhus N., Debattista V. P., Pannella M., Méndez R. H., 2008, *MNRAS*, 385, 1729
- de Zeeuw P. T., 1985, *MNRAS*, 216, 273
- Dehnen W., Gerhard O. E., 1994, *MNRAS*, 268, 1019
- Dubois Y., Gavazzi R., Peirani S., Silk J., 2013, *MNRAS*, 433, 3297
- Emsellem E., Cappellari M., Krajnović D., Alatalo K., Blitz L., Bois M., Bournaud F., Bureau M., Davies R. L., Davis T. A., de Zeeuw P. T., Khochfar S., 2011, *MNRAS*, 414, 888
- Emsellem E., Cappellari M., Krajnović D., van de Ven G., Bacon R., Bureau M., Davies R. L., de Zeeuw P. T., Falcón-Barroso J., Kuntschner H., McDermid R., Peletier R. F., Sarzi M., 2007, *MNRAS*, 379, 401
- Feldmann R., Carollo C. M., Mayer L., 2011, *ApJ*, 736, 88
- Fisher D., 1997, *AJ*, 113, 950
- Fogarty L. M. R., Bland-Hawthorn J., Croom S. M. e. a., 2012, *ApJ*, 761, 169
- Gerhard O. E., 1993, *MNRAS*, 265, 213
- Guo Q., White S. D. M., 2008, *MNRAS*, 384, 2
- Halliday C., Davies R. L., Kuntschner H., Birkinshaw M., Bender R., Saglia R. P., Baggle G., 2001, *MNRAS*, 326, 473
- Hernquist L., 1990, *ApJ*, 356, 359
- Hernquist L., Ostriker J. P., 1992, *ApJ*, 386, 375
- Heyl J. S., Hernquist L., Spergel D. N., 1994, *ApJ*, 427, 165
- Hill G. J., MacQueen P. J., Smith M. P. e. a., 2008, in *Society of Photo-Optical Instrumentation Engineers (SPIE) Conference Series Vol. 7014 of Society of Photo-Optical Instrumentation Engineers (SPIE) Conference Series*, Design, construction, and performance of VIRUS-P: the prototype of a highly replicated integral-field spectrograph for HET
- Hilz M., Naab T., Ostriker J. P., 2013, *MNRAS*, 429, 2924
- Hirschmann M., Naab T., Davé R., Oppenheimer B. D., Ostriker J. P., Somerville R. S., Oser L., Genzel R., Tacconi L. J., Förster-Schreiber N. M., Burkert A., Genel S., 2013, *MNRAS*, 436, 2929
- Hirschmann M., Naab T., Somerville R. S., Burkert A., Oser L., 2012, *MNRAS*, 419, 3200
- Hoffman L., Cox T. J., Dutta S., Hernquist L., 2009, *ApJ*, 705, 920
- Hoffman L., Cox T. J., Dutta S., Hernquist L., 2010, *ApJ*, 723, 818
- Jesseit R., Naab T., Burkert A., 2005, *MNRAS*, 360, 1185
- Johansson P. H., Naab T., Ostriker J. P., 2012, *ApJ*, 754, 115
- Khochfar S., Silk J., 2006, *ApJL*, 648, L21
- Kolmogorov A. N., 1954, *Dokl. Akad. Nauk SSSR*, 98, 525
- Kolmogorov A. N., 1979, *LNP*, 93, 51
- Krajnović D., Alatalo K., Blitz L. e. a., 2013, *MNRAS*, 432, 1768
- Krajnović D., Bacon R., Cappellari M., Davies R. L., de Zeeuw P. T., Emsellem E., Falcón-Barroso J., Kuntschner H., McDermid R. M., Peletier R. F., Sarzi M., van den Bosch R. C. E., van de Ven G., 2008, *MNRAS*, 390, 93
- Krajnović D., Emsellem E., Cappellari M. e. a., 2011, *MNRAS*, 414, 2923
- Lackner C. N., Cen R., Ostriker J. P., Joung M. R., 2012, *MNRAS*, 425, 641
- Lyskova N., Churazov E., Zhuravleva I., Naab T., Oser L., Gerhard O., Wu X., 2012, *MNRAS*, 423, 1813
- Ma C.-P., Greene J. E., McConnell N., Janish R., Blakeslee J. P., Thomas J., Murphy J. D., 2014, *ArXiv e-prints*
- Mo H. J., Mao S., White S. D. M., 1998, *MNRAS*, 295, 319
- Moser J., ed. 1973, *Stable and random motions in dynamical systems. With special emphasis on celestial mechanics*
- Moster B. P., Naab T., White S. D. M., 2013, *MNRAS*, 428, 3121
- Moster B. P., Somerville R. S., Maulbetsch C. e. a., 2010, *ApJ*, 710, 903
- Naab T., 2013, in *Thomas D., Pasquali A., Ferreras I., eds, IAU Symposium Vol. 295 of IAU Symposium, Modelling the formation of today's massive ellipticals*. pp 340–349
- Naab T., Burkert A., 2001, *ApJL*, 555, L91
- Naab T., Burkert A., 2003, *ApJ*, 597, 893
- Naab T., Jesseit R., Burkert A., 2006, *MNRAS*, 372, 839
- Naab T., Johansson P. H., Ostriker J. P., 2009, *ApJL*, 699, L178
- Naab T., Johansson P. H., Ostriker J. P., Efstathiou G., 2007, *ApJ*, 658, 710
- Naab T., Oser L., Emsellem E. e. a., 2013, *arXiv:1311.0284*
- Naab T., Trujillo I., 2006, *MNRAS*, 369, 625
- Oser L., Naab T., Ostriker J. P., Johansson P. H., 2012, *ApJ*, 744, 63
- Oser L., Ostriker J. P., Naab T., Johansson P. H., Burkert A., 2010, *ApJ*, 725, 2312
- Pinkney J., Gebhardt K., Bender R., Bower G., Dressler A., Faber S. M., Filippenko A. V., Green R., Ho L. C., Kormendy J., Lauer T. R., Magorrian J., Richstone D.,

- Tremaine S., 2003, *ApJ*, 596, 903
- Piontek F., Steinmetz M., 2011, *MNRAS*, 410, 2625
- Power C., Navarro J. F., Jenkins A., Frenk C. S., White S. D. M., Springel V., Stadel J., Quinn T., 2003, *MNRAS*, 338, 14
- Puchwein E., Springel V., 2013, *MNRAS*, 428, 2966
- Sánchez S. F., Kennicutt R. C., Gil de Paz A. e. a., 2012, *A&A*, 538, A8
- Scannapieco C., Wadepuhl M., Parry O. H., Navarro J. F., Jenkins A., Springel V., Teyssier R., Carlson E., Couchman H. M. P., Crain R. A., 2012, *MNRAS*, 423, 1726
- Sharples R., Bender R., Bennett R. e. a., 2006, *New Astronomy Reviews*, 50, 370
- Spergel D. N., Bean R., Doré O. e. a., 2007, *ApJ*, 170, 377
- Springel V., 2005, *MNRAS*, 364, 1105
- Springel V., Hernquist L., 2003, *MNRAS*, 339, 289
- Springel V., Yoshida N., White S. D. M., 2001, *Nature*, 6, 79
- Statler T. S., 1987, *ApJ*, 321, 113
- Thomas J., Saglia R. P., Bender R., Thomas D., Gebhardt K., Magorrian J., Corsini E. M., Wegner G., 2007, *MNRAS*, 382, 657
- Übler H., Naab T., Oser L., Aumer M., Sales L. V., White S., 2014, *arXiv:1403.6124*
- van de Ven G., van den Bosch R. C. E., Verolme E. K., de Zeeuw P. T., 2006, *A&A*, 445, 513
- van den Bosch R. C. E., van de Ven G., Verolme E. K., Cappellari M., de Zeeuw P. T., 2008, *MNRAS*, 385, 647
- van der Marel R. P., Franx M., 1993, *ApJ*, 407, 525
- Villumsen J. V., 1982, *MNRAS*, 199, 493
- Weijmans A.-M., Cappellari M., Bacon R., de Zeeuw P. T., Emsellem E., Falcón-Barroso J., Kuntschner H., McDermid R. M., van den Bosch R. C. E., van de Ven G., 2009, *MNRAS*, 398, 561
- Wu X., Gerhard O., Naab T., Oser L., Martinez-Valpuesta I., Hilz M., Churazov E., Lyskova N., 2014, *MNRAS*, 438, 2701